University of Groningen

Spitzer Mid-IR Spectroscopy of Powerful 2 Jy and 3CRR Radio Galaxies

Dicken, D.; Tadhunter, C.; Axon, D.; Morganti, R.; Robinson, A.; Kouwenhoven, M. B. N.; Spoon, H.; Kharb, P.; Inskip, K. J.; Holt, J.

Published in:
Astrophysical Journal

DOI:
10.1088/0004-637X/745/2/172

IMPORTANT NOTE: You are advised to consult the publisher's version (publisher's PDF) if you wish to cite from it. Please check the document version below.

Document Version
Publisher's PDF, also known as Version of record

Publication date:
2012

Link to publication in University of Groningen/UMCG research database

Citation for published version (APA):
Dicken, D., Tadhunter, C., Axon, D., Morganti, R., Robinson, A., Kouwenhoven, M. B. N., Spoon, H., Kharb, P., Inskip, K. J., Holt, J., Almeida, C. R., & Nesvadba, N. P. H. (2012). Spitzer Mid-IR Spectroscopy of Powerful 2 Jy and 3CRR Radio Galaxies: I. Evidence against a Strong Starburst-AGN Connection in Radio-loud AGN. *Astrophysical Journal*, *745*(2), 172-192. https://doi.org/10.1088/0004-637X/745/2/172

Copyright
Other than for strictly personal use, it is not permitted to download or to forward/distribute the text or part of it without the consent of the author(s) and/or copyright holder(s), unless the work is under an open content license (like Creative Commons).

The publication may also be distributed here under the terms of Article 25fa of the Dutch Copyright Act, indicated by the “Taverne” license. More information can be found on the University of Groningen website: https://www.rug.nl/library/open-access/self-archiving-pure/taverne-amendment.

Take-down policy
If you believe that this document breaches copyright please contact us providing details, and we will remove access to the work immediately and investigate your claim.

Downloaded from the University of Groningen/UMCG research database (Pure): http://www.rug.nl/research/portal. For technical reasons the number of authors shown on this cover page is limited to 10 maximum.

Download date: 27-08-2022

The Astrophysical Journal, 745:172 (21pp), 2012 February 1
doi:10.1088/0004-637X/745/2/172

SPITZER MID-IR SPECTROSCOPY OF POWERFUL 2 JY AND 3CRR RADIO GALAXIES. I. EVIDENCE AGAINST A STRONG STARBURST–AGN CONNECTION IN RADIO-LOUD AGN

D. Dicken[1], C. Tadhunter[2], D. Axon[1,3], R. Morganti[4,5], A. Robinson[1], M. B. N. Kouwenhoven[6], H. Spoon[7], P. Kharb[1], K. J. Inskip[8], J. Holt[9], C. Ramos Almeida[2], and N. P. H. Nesvadba[10]
[1] Rochester Institute of Technology, 84 Lomb Memorial Drive, Rochester, NY 14623, USA; daniel.dicken@ias.u-psud.fr
[2] Department of Physics and Astronomy University of Sheffield, Hounsfield Road, Sheffield, S3 7RH, UK
[3] Department of Physics and Astronomy University of Sussex, Pevensey 2, Falmer, Brighton, BN1 9QH, UK
[4] ASTRON, P.O. Box 2, 7990 AA Dwingeloo, The Netherlands
[5] Kapetyn Astronmical Institute, University of Groningen, Postbuss 800, 9700 AV Groningen, The Netherlands
[6] Kavli Institute for Astronomy and Astrophysics, Peking University, Yi He Yuan Lu 5, Haidian Qu, Beijing 100871, China
[7] 224 Space Sciences Building, Cornell University, Ithaca, NY 14853, USA
[8] Max Planck Institute for Astronomy, Königstuhl 17, 69117 Heidelberg, Germany
[9] Leiden Observatory, Leiden University, P.O. Box 9513, 2300 RA Leiden, The Netherlands
[10] Institut d'Astrophysique Spatiale, CNRS, Université Paris Sud, 91405 Orsay, France
Received 2011 April 1; accepted 2011 November 10; published 2012 January 16

ABSTRACT

We present deep *Spitzer*/Infrared Spectrograph (IRS) spectra for complete samples of 46 2 Jy radio galaxies ($0.05 < z < 0.7$) and 19 3CRR FRII radio galaxies ($z < 0.1$), and use the detection of polycyclic aromatic hydrocarbon (PAH) features to examine the incidence of contemporaneous star formation and radio-loud active galactic nucleus (AGN) activity. Our analysis reveals PAH features in only a minority (30%) of the objects with good IRS spectra. Using the wealth of complementary data available for the 2 Jy and 3CRR samples we make detailed comparisons between a range of star formation diagnostics: optical continuum spectroscopy, mid- to far-IR (MFIR) color, far-IR excess and PAH detection. There is good agreement between the various diagnostic techniques: most candidates identified to have star formation activity on the basis of PAH detection are also identified using at least two of the other techniques. We find that only 35% of the combined 2 Jy and 3CRR sample show evidence for recent star formation activity (RSFA) at optical and/or MFIR wavelengths. This result argues strongly against the idea of a close link between starburst and powerful radio-loud AGN activity, reinforcing the view that, although a large fraction of powerful radio galaxies may be triggered in galaxy interactions, only a minority are triggered at the peaks of star formation activity in major, gas-rich mergers. However, we find that compact radio sources ($D < 15$ kpc) show a significantly higher incidence of RSFA (>75%) than their more extended counterparts (≈15%–25%). We discuss this result in the context of a possible bias toward the selection of compact radio sources triggered in gas-rich environments.

Key words: galaxies: active – infrared: galaxies

Online-only material: color figures

1. INTRODUCTION

Extragalactic radio sources form an important subset of the active galactic nucleus (AGN) population because their relativistic jets heat the interstellar/galactic medium (ISM/IGM) and drive outflows on scales ranging from the kpc-scale narrow-line regions (NLR; Holt et al. 2008), to the 100 kpc–1 Mpc hot X-ray halos of the host galaxies and galaxy clusters (McNamara & Nulsen 2007). Such feedback has been used to explain the cooling problem for the hot X-ray gas (Best et al. 2005), as well as the high end shape of the galaxy luminosity function (Benson et al. 2003), and the correlations between black hole mass and host galaxy properties (Bower et al. 2006; Croton et al. 2006). Therefore, given that a large percentage of giant elliptical galaxies may go through a radio-loud phase (Best et al. 2006), the triggering of radio galaxies is a key issue for the understanding of the evolution of massive galaxies in general. However, there remain considerable uncertainties about how and when radio-loud AGN activity is triggered.

Morphological and spectroscopic studies provide strong evidence that powerful radio galaxies are triggered in galaxy mergers, although not necessarily at a single phase of a particular type of merger (Heckman et al. 1986; Ramos Almeida et al. 2011, 2012; Tadhunter et al. 2011). Given that hydrodynamic simulations of major, gas-rich mergers show that, as well as triggering AGN, such interactions are capable of triggering powerful starburst activity (Mihos & Hernquist 1996; Di Matteo et al. 2007; Cox et al. 2008; Johansson et al. 2009), the study of the level of recent star formation activity (hereafter RSFA)[11] in radio galaxies provides key information about the nature of the triggering events, as well as the timing of the AGN relative to any merger-induced starburst.

The fact that radio-loud AGNs are overwhelmingly hosted by early-type galaxies allows particularly clean searches to be made for the signs of RSFA. Perhaps surprisingly, given the evidence that many of them have been involved in galaxy interactions (Heckman et al. 1986; Ramos Almeida et al. 2011, 2012), only a minority of radio galaxies are found to show spectroscopic evidence for RSFA at optical wavelengths (Tadhunter et al. 2002, 2011). However, it is possible that a substantial percentage of any star formation activity is obscured at short wavelengths by circumnuclear dust. Moreover, in some

---

[11] We define "recent star formation activity" to include all star formation activity that has occurred within 2 Gyr of the observation epoch, encompassing contemporaneous starbursts, continuous star formation, and post-starburst stellar populations (e.g., post-starburst activity as detected in spectral synthesis modeling of optical spectra: Tadhunter et al. 2005; Holt et al. 2007; Tadhunter et al. 2011).

cases the optical continuum features that are characteristic of RSFA may be masked by AGN-related continuum emission components such as direct or scattered AGN light, and nebular continuum (Tadhunter et al. 2002). Clearly, it is important to explore star formation diagnostics that are less sensitive to dust extinction and AGN-related continuum emission. Therefore, we are undertaking a program to investigate the degree of RSFA in radio galaxies using mid- to far-IR (MFIR) diagnostics.

As a first step we used the Multiband Imaging Photometer for *Spitzer* (MIPS; Rieke et al. 2004) to make deep MFIR photometry measurements of the complete 2 Jy sample of 46 radio-loud AGN ($0.05 < z < 0.7$) (Program 20233: PI Tadhunter; Tadhunter et al. 2007; Dicken et al. 2008, 2009, hereafter T07, D08, D09) as well as a sample of 19 nearby 3CRR radio-loud AGN from the *Spitzer* archive (Dicken et al. 2010, hereafter D10). The results show that [O III]λ5007 optical emission line luminosity ($L_{[\mathrm{O\,III}]}$) is strongly correlated with both the mid- (24 μm) and far-IR (70 μm) luminosities ($L_{24\,\mu\mathrm{m}}$ and $L_{70\,\mu\mathrm{m}}$, respectively). Since the [O III] emission from the NLR provides a good indication of the intrinsic power of the illuminating AGN (e.g., Rawlings & Saunders 1991; Tadhunter et al. 1998; Simpson 1998; LaMassa et al. 2010; and discussion in D09), the correlations between MFIR luminosity and [O III] optical emission line luminosity provide strong empirical evidence to support AGN illumination as the dominant heating mechanism of the thermal MFIR emitting dust. We also used energetic arguments to demonstrate that, while much of the mid-IR emission is likely to be radiated by the warm dust in the torus, the NLR clouds are a plausible location for the cooler, far-IR emitting dust (D09).

In addition, we found evidence for enhanced far-IR emission in the minority of radio galaxies that show evidence for RSFA activity at optical wavelengths. Our interpretation was that, while AGN illumination is the primary heating mechanism for both the warm (mid-IR emitting, 24 μm) and cool (far-IR emitting, 70 μm) dust in most powerful radio-loud AGN, heating by starbursts acts to substantially boost the 70 μm luminosity in the 20%–30% of objects in the 2 Jy sample with optical evidence for RSFA.

Unfortunately, apart from the most extreme objects with the highest degrees of star formation activity, the far-IR excess does not necessarily provide an accurate indication of the level of star formation activity in individual radio galaxies. This is because the degree of contamination of the far-IR continuum by emission from the NLR and circumnuclear torus may vary substantially from object to object. An alternative is to use mid-IR spectroscopy to detect the strong polycyclic aromatic hydrocarbon (PAH) emission features at 6.2, 7.7, 8.6, and 11.3 μm. These well-defined emission bands are considered to provide an unambiguous signature of RSFA (Diamond-Stanic & Rieke 2010) and are much less susceptible to dust extinction effects than optical continuum studies.

Therefore, we have undertaken a campaign to observe the complete 2 Jy sample of 46 objects ($0.05 < z < 0.7$), previously observed with *Spitzer*/MIPS, using the *Spitzer* Infrared Spectrograph (IRS: Houck et al. 2004; program 50588: PI Tadhunter). In a similar manner to the work presented in D10, we also examine IRS spectra for a complete sample of 19 3CRR FRII radio galaxies that have, on average, lower redshifts and radio powers than the 2 Jy sample.

We aim to investigate the degree to which the presence and strength of the PAH emission features correlates with other diagnostics for identifying RSFA. In particular: is the detection of PAH features, and therefore RSFA by association, confined to the objects in which we already find evidence for such activity at optical wavelengths? Or is there a substantial population of radio galaxies in which the star formation activity is hidden by dust and/or masked by AGN-related continuum components at optical wavelengths?

In this, the first paper related to our IRS program of spectral observations of powerful radio galaxies, we present an atlas of *Spitzer* IRS mid-IR spectra for the 2 Jy and 3CRR samples, and discuss the results from the PAH emission analysis. In a second paper we will discuss the silicate features and fine-structure lines detected in the spectra in the context of the unified schemes for AGN. We assume a cosmology with $H_o = 71\,\mathrm{km\,s^{-1}\,Mpc^{-1}}$, $\Omega_m = 0.27$, and $\Omega_\lambda = 0.73$ throughout this work.

2. SAMPLE SELECTION

The primary sample consists of all 46 powerful radio galaxies and steep-spectrum quasars ($F_\nu \propto \nu^{-\alpha}$, $\alpha_{2.7}^{4.8} > 0.5$) selected from the 2 Jy sample of Wall & Peacock (1985) with redshifts $0.05 < z < 0.7$, flux densities $S_{2.7\,\mathrm{GHz}} > 2$ Jy, and declinations $\delta < 10°$; the sample is complete based on these criteria. This sample is identical to that presented in Tadhunter et al. (1993) and Morganti et al. (1993) except that the redshift and steep-spectrum selection criteria have been applied, and the object PKS 0347+05, which has since proved to fulfill the same selection criteria (di Serego-Alighieri et al. 1994), has been added. The spectral index cut has been set to ensure that all the sources in the sample are dominated by steep-spectrum lobe emission, while the lower redshift limit has been set to ensure that these galaxies are genuinely powerful sources. In the following we will refer to this sample as the 2 Jy sample.

The mid-IR spectra presented here complement a wealth of data that has been obtained for the 2 Jy sample over the last two decades. These include the following: deep optical spectroscopic observations (Tadhunter et al. 1993, 1998, 2002; Wills et al. 2002; Holt et al. 2007); extensive observations at radio wavelengths (Morganti et al. 1993, 1997, 1999; D08); complete deep optical imaging from Gemini (Ramos Almeida et al. 2011, 2012); and deep *Spitzer*/MIPS MFIR photometric observations (D08; detection rates 100% at 24 μm and 90% at 70 μm). In addition, 85% of the sample have recently been observed with *Chandra* and/or *XMM* at X-ray wavelengths, including all objects with redshifts $z < 0.2$; and 78% of the sample have deep 2.2 μm (*K*-band) near-infrared imaging (Inskip et al. 2010). The full sample of 46 objects includes a mixture of broad-line radio galaxies and radio-loud quasars (BLRG/Q: 35%), narrow-line radio galaxies (NLRG: 43%), and weak-line radio galaxies[12] (WLRG: 22%). In terms of radio morphological classification, the sample comprises 72% FRII sources, 13% FRI sources, and 15% compact steep-spectrum (CSS)/gigahertz peak spectrum (GPS) objects. The sample is presented in Table 1.[13]

We also present IRS spectra for a complete sub-sample of 19 3CRR radio-loud AGN selected from the sample of Laing et al. (1983; see Table 2). We have limited this sample to 3CRR objects with FRII radio morphologies and redshifts $z \leqslant 0.1$,

---

[12] WLRGs are defined as having EW ([O III]) <10 Å (Tadhunter et al. 1998).

[13] Additional information on these objects and the more extended 2 Jy sample can be found at http://2jy.extragalactic.info.

Table 1

The 2 Jy Sample—*Spitzer* Observational Data

Name	Other Name	z	Mode	Obs. Date	t_{int}(SL1)	Cycles	t_{int}(SL2)	Cycles	t_{int}(LL1)	Cycles	t_{int}(LL2)	Cycles	xSL
0023−26		0.322	S	Jan 9	60	8	60	8	120	4	120	4	...
0034−01	3C15	0.073	S	Jan 6	240	2	240	3	120	3	120	2	0.8
0035−02	3C17	0.220	S	Jan 6	240	2	240	3	120	3	120	2	...
0038 + 09	3C18	0.188	S	Jan 9	14	16	14	16	30	4	30	4	...
0039−44		0.346	S	Dec 8	60	4	60	4	30	4	30	4	1.1
0043−42		0.116	S	Dec 8	60	4	60	4	120	2	120	2	...
0105−16	3C32	0.400	S	Jan 9	60	4	60	4	120	2	120	2	...
0117−15	3C38	0.565	S	Jan 9	60	8	60	8	120	4	120	4	...
0213−13	3C62	0.147	S	Jan 9	60	2	60	2	30	4	30	4	1.1
0235−19	OD-159	0.620	S	Oct 8	60	4	60	4	120	2	120	2	...
0252−71		0.566	S	Oct 8	240	2	240	2	120	4	120	4	...
0347 + 05		0.339	S	Oct 8	60	8	60	8	120	4	120	4	...
0349−27		0.066	S	Oct 8	60	4	60	4	120	2	120	2	...
0404 + 03	3C105	0.089	M	Sep 5	14	1	14	1	14	1	14	1	...
0409−75		0.693	S	Dec 8	240	2	240	2	120	4	120	4	...
0442−28		0.147	S	Nov 8	60	4	60	4	30	4	30	4	...
0620−52		0.051	S	Dec 8	240	2	240	2	120	3	120	3	1.2
0625−35	OH-342	0.055	S	Dec 8	60	2	60	2	30	4	30	4	1.1
0625−53		0.054	S	Dec 8	240	2	240	2	120	4	120	4	...
0806−10	3C195	0.110	S	Dec 8	14	4	6	2	6	2	6	2	1.1
0859−25		0.305	S	Jan 9	60	4	60	4	120	2	120	2	1.3
0915−11	Hydra A	0.054	S	Dec 5	60	9	60	11	30	4	30	4	3.0
0945 + 07	3C227	0.086	M	May 6	14	1	14	1	14	1	14	1	1.2
1136−13		0.554	S	Jul 8	60	4	60	4	120	2	120	2	...
1151−34		0.258	S	Feb 9	60	2	60	2	30	4	30	4	
1306−09		0.464	S	Aug 8	14	32	14	32	120	3	120	3	...
1355−41		0.313	S	Mar 9	60	2	60	2	30	4	30	4	1.1
1547−79		0.483	S	Oct 8	60	4	60	4	120	2	120	2	1.1
1559 + 02	3C327	0.104	S	Oct 8	14	4	6	2	6	2	6	2	1.1
1602 + 01	3C327.1	0.462	S	Mar 6	240	2	240	3	120	3	120	2	...
1648 + 05	Herc A	0.154	S	...	...	...	...	...	...	...	...	...	...
1733−56		0.098	S	Oct 8	60	2	60	2	30	2	30	2	...
1814−63		0.063	S	Nov 8	60	2	60	2	30	2	20	2	1.1
1839−48		0.112	S	Nov 8	60	6	60	6	120	4	120	4	...
1932−46		0.231	S	Nov 8	60	8	60	8	120	4	120	4	0.7
1934−63		0.183	S	Nov 8	60	4	60	4	30	4	30	4	...
1938−15		0.452	S	Nov 8	14	16	14	16	120	2	120	2	1.8
1949 + 02	3C403	0.059	M	Oct 5	14	1	14	1	14	1	14	1	...
1954−55		0.060	S	Nov 8	60	6	60	6	120	4	120	4	...
2135−14		0.200	S	...	...	...	...	...	...	...	...	...	...
2135−20	OX-258	0.635	S	Nov 8	14	28	14	28	120	4	120	4	...
2211−17	3C444	0.153	S	...	...	...	...	...	...	...	...	...	...
2221−02	3C445	0.057	S	Jun 4	30	4	60	2	14	2	14	2	1.2
2250−41		0.310	S	Nov 8	60	4	60	4	120	3	120	3	...
2314 + 03	3C459	0.220	S	Jan 9	14	16	14	16	30	2	30	2	...
2356−61		0.096	S	Nov 8	60	4	60	4	30	4	30	4	...

Notes. Table presenting the basic parameters for the 2 Jy sample as well as details of the *Spitzer*/IRS observations. Column 4 presents the IRS observing mode—S: staring mode; M: mapping mode. Integration time in seconds and cycles for the *IRS* observations are presented in Columns 6–13. SL1: 5.2−8.7 μm; SL2: 7.4−14.5 μm; LL1: 14−21.3 μm; LL2:19.5−38 μm. Column 14 presents the multiplication factor applied to the SL spectrum in order to match the LL spectrum where applicable.

leading to a sample which is complete in both *Spitzer*/MIPS detections (100% at 24 μm and 89% at 70 μm) and [O III] λ5007 emission line flux measurements (100%). The full sample of 19 objects also includes a mixture of BLRG/Q (16%), NLRG (58%), and WLRG (26%). Because the 3CRR objects have lower radio powers and redshifts on average than most of the 2 Jy sample, they help to fill in the lower luminosity ends of the MFIR versus [O III] correlations (D10). In the following discussion we will refer to this sample as the 3CRR sample. Note that, although two objects in the sample (3C277.3, 3C293) have uncertain radio morphological classifications and cannot be confidently characterized as either FRI or FRII types, they are included here for completeness. Also, the CSS radio source 3C305 is included because it presents a miniature FRII radio morphology, with distinct hot spots at the ends of its jets, even if its radio structure as a whole is highly distorted because of strong jet–cloud interactions (Heckman et al. 1982). The *Spitzer*/MIPS flux data and associated errors are presented in D10. The [O III] fluxes were obtained from published deep optical spectra at both high and low resolution taken using Dolores on the Telescope Nazionale Galileo (Buttiglione et al. 2009), except for DA240, 4C73.08, 3C321, and 3C445 (see D10 for details). Note that two objects overlap between the 3CRR and 2 Jy samples (3C403, 3C445).

Table 2
The 3CRR Sample—*Spitzer* Observational Data

Name	z	Mode	Obs. Date	t_{int}(SL1)	Cycles	t_{int}(SL2)	Cycles	t_{int}(LL1)	Cycles	t_{int}(LL2)	Cycles	xSL
3C33	0.060	S	Jan 5	60	2	60	2	120	2	120	1	1.03
3C35	0.067	M	Jan 6	14	1	14	1	14	1	14	1	…
3C98	0.030	M	Sep 6	14	1	14	1	14	1	14	1	…
DA240	0.036	…	…	…	…	…	…	…	…	…	…	…
3C192	0.060	S	Nov 5	60	2	60	2	120	2	120	1	…
4C73.08	0.058	…	…	…	…	…	…	…	…	…	…	…
3C236	0.101	M	Dec 5	14	1	14	1	14	1	14	1	…
3C277.3	0.085	…	Jan 6	14	1	14	1	14	1	14	1	…
3C285	0.079	M	Jan 6	14	1	14	1	14	1	14	1	…
3C293	0.045	S	Jan 6	240	2	240	3	120	3	120	2	1.2
3C305	0.042	M	Apr 6	14	1	14	1	14	1	14	1	…
3C321	0.096	S	Feb 5	14	2	14	2	30	1	30	1	…
3C326	0.090	S	Mar 5	60	2	60	2	120	2	120	1	…
3C382	0.058	S	Aug 5	60	2	60	2	120	2	120	1	1.2
3C388	0.092	S	Jul 5	60	2	60	2	120	2	120	1	1.5
3C390.3	0.056	S	Aug 4	240	1	240	1	120	4	120	4	0.96
3C452	0.081	S	Dec 4	60	2	60	2	120	2	120	1	…

Notes. Table presenting the basic parameters for the 3CRR sample as well as details of the *Spitzer*/IRS observations. Note that 3C403 and 3C445 overlap between the two samples, see Table 1 for observation details of these two objects. Definitions are the same as Table 1.

3. OBSERVATIONS AND DATA REDUCTION

The mid-IR spectra of 35 out of the 46 objects in the 2 Jy sample were obtained in a dedicated campaign of *Spitzer* IRS observations (program 50558: PI Tadhunter) between 2008 July and 2009 March. These data were taken in the short low (SL) and long low (LL) resolution staring modes, covering 5.2–14.5 μm and 14.0–38.0 μm, respectively. The resolution for the observations was $R \approx 60$–127 and the slit widths were $3\farcs6$ and $10\farcs5$ for the SL and LL observations, respectively. The spectra of eight additional objects in the 2 Jy sample, taken between 2004 June and 2006 May, were obtained from the *Spitzer* archive. These data came from various campaigns under several different PIs and, consequently, have varying integration times and observing modes. Details of the observations can be found in Table 1.

Out of the 46 objects in the 2 Jy sample, 43 (93%) were successfully detected by *Spitzer*/IRS. PKS2135−14 was not observed because the *Spitzer* observatory ran out of cryogenic coolant before the observations could be made, while no observations of PKS2211−17 were taken because its mid-IR flux level (0.5 mJy at 24 μm) was deemed too low to detect in reasonable integrations with *Spitzer* IRS. Observations of a further object (PKS1648+05) were available in the *Spitzer* archive, however, the integration times were an order of magnitude lower than those used for objects of similar mid-IR flux in our program. Therefore, this source was not detected with the IRS instrument. The SL spectra of an additional three objects (PKS0034−01, PKS0035−02, PKS1602+01) obtained from the *Spitzer* archive potentially suffer from higher flux calibration uncertainties, due to the effect of saturation of part of the detector used for the short-wavelength range observations. This problem occurs because the *IRS* detectors encompass not only the spectral two-dimensional images, but also the apertures used for the target acquisition imaging. If the ambient infrared background is high (above 25 mJy sr^{-1}) then, for long integration times, the acquisition images are likely to saturate, causing the whole detector to perform irregularly.

The majority of observations (40/43) were taken in staring mode, in which the target is observed in several cycles of set integration time and, for each cycle, the *IRS* instrument nods the object between two positions on the detector. For every cycle the nod positions were subtracted (A from B, and B from A) in order to perform background subtraction on the image, as well as to counteract intrinsic sensitivity variations across the detector. The two resulting spectra were combined to produce the final spectrum.

Spectra for three 2 Jy sources, obtained from the *Spitzer* archive, were observed in mapping mode in which the spacecraft makes a pre-determined number of pointings of set integration time mapped over a target. The pattern can be varied, however, these three objects were all part of the same program (program 20719: PI Baum) and the observational patterns were identical. All pointings had an integration time of 14 s, with 15 and 5 pointings for the SL and LL modules, respectively. The middle number (i.e., 8 in SL, and 3 in LL) pointing was centered on the target and, since these objects are relatively bright at MFIR wavelengths, this single central observation was used to extract the spectrum of each object. Because of the relatively short exposure times of the single exposures centered on the targets, these mapping mode observations tend to have a lower signal-to-noise ratio (S/N) than the staring mode observations used for the majority of the sample. In order to subtract the background, a median image of the other pointed observations was made, and we took this median image to represent the sky spectrum, subtracting this from the central pointing observation. To reduce the possibility of removing flux from the source in this process, we avoided using those pointed observations directly either side of the central pointing in the sky image (i.e., spectra 7 and 9 for SL, 2 and 4 for LL). Overall, the continuum level of the mapping mode data matched well with the continuum measurement from *Spitzer* MIPS data measured over the 24 μm spectral filter response range (see below for further discussion).

All the data were downloaded in the basic calibrated data format processed with the S18.7.0 data pipeline. These data were combined and subtracted using our own IDL code and cleaned using the SSC software IRSCLEAN MASK. The data were extracted using SMART (v.8.1.2.) program developed by the IRS Team at Cornell University (Higdon et al. 2004; Lebouteiller et al. 2010). To extract the fluxes we employed the optimal extraction function which uses a super sampled point-spread function and weights the extracted spectra by the S/N of each pixel (Lebouteiller et al. 2010), assuming that the objects are unresolved point sources at these wavelengths. The extracted spectra from both nod positions were compared by eye, and further cleaning by hand was performed where necessary, i.e., by averaging over obvious strong sharp features that only appeared in one nod position. These spectra were then averaged together to produce the final spectrum. Note that the IRS pipeline automatically accounts for variable slit losses with wavelength.

Seventeen of the 19 objects in the 3CRR sample have been observed with *Spitzer*/IRS. Two objects were not observed (4C73.08 and DA240) and the S/N of the data for 3C35 and 3C277.3 was too low to extract science quality data. Therefore, 15/19 objects (79%) have good IRS data. The data were reduced in an identical manner to that described for the 2 Jy sample; five objects were observed in mapping mode and the rest in staring mode. Details of the observations can be found in Table 2.

For the majority of the resulting spectra (63%) the continuum level of the SL spectrum matched well with that of the LL spectrum. This demonstrates that the extraction techniques and background subtraction method are robust for most objects, and that the sources are not spatially extended. However, for 15 objects in the 2 Jy sample and 2 objects in the 3CRR sample, the SL spectrum and LL spectrum did not precisely match when we attempted to combine them together. The likely causes of this flux difference include the objects being partially extended, pointing errors, or poor calibration due to peak-up saturation of the detector (discussed above). For most of these objects we applied a scaling factor to the SL spectrum of between 0.8 and 1.15,[14] where the median scaling factor was 1.1 (see Tables 1 and 2). We kept the flux level of the LL spectrum constant because the LL slit width is larger and therefore more likely to include the entire flux from any sources that are partially extended, or not perfectly centered.

The spatially integrated 24 μm flux values obtained from our *Spitzer*/MIPS photometric campaign can be used to check the flux calibration of the *Spitzer*/IRS data. The mean flux from the IRS spectra was calculated over the response range of the 24 μm filter for MIPS in the observed frame. We found that the estimated IRS fluxes agree to within 15% of the measured MIPS 24 μm photometric values for all the sources, with a median of the ratio of $\mathrm{MIPS}_{24\,\mu\mathrm{m}}$ to $\mathrm{IRS}_{24\,\mu\mathrm{m}}$ of 0.94. This provides evidence that our spectra capture the majority of the mid-IR emission associated with any star formation in the host galaxies of the radio sources.

Overall, we have usable IRS spectra for 56 (89%) of the 63 objects in the combined 2 Jy and 3CRR sample.

4. DATA ANALYSIS

The fully reduced rest-frame spectra for the 43 observed/detected objects in the 2 Jy sample and the 13 objects from the 3CRR sample (not in common with the 2 Jy sample) are presented in Figures 1 through 6. The IRS spectral range is 5–38 μm, however, at longer wavelengths the S/N is low. Therefore, we present the spectra only up to 30 μm in the observed frame and/or 27 μm in the rest frame.

The diversity in the spectra of the radio sources shown in Figures 1 through 6 is striking. Many of the objects show the characteristic features of AGN at mid-IR wavelengths, including strong fine-structure emission lines, as well as weak silicate emission or absorption features (Hao et al. 2007). We have identified some of the most prominent fine-structure lines on the spectral plots: [Ne VI]λ7.65 μm, [Ar III]λ8.99 μm, [S IV]λ10.51 μm, [Ne II]λ12.81 μm, [Ne V]λ14.32 μm, [Ne III]λ15.56 μm, [S III]λ18.71 μm, [Ne V]λ24.31 μm, and [O IV]λ25.89 μm. We also indicate the location of H_2 lines (S(1) through S(6)).[15] It is noteworthy that nearly all the spectra show the high ionization [O IV]λ25.89 μm ($E_{\mathrm{ion}} = 54.9$ eV) emission, when not redshifted outside the observable wavelength range. This indicates a high ionization state, as expected given the presence of powerful AGN in many of the sources. Low ionization potential lines such as [Ne II]λ12.81 μm ($E_{\mathrm{ion}} = 21.6$ eV) are also detected in many spectra. The contribution of starlight from the host galaxies is significant at short wavelengths ($\lambda < 8\,\mu$m) in some low-redshift objects, seen as a sharp upturn in flux at the blue end of the spectra. This is particularly apparent for objects with low power AGN, for example, the WLRG PKS1839−48 and PKS1954−55 (see Figure 4). The fine-structure, H_2, and silicate emission/absorption features will be discussed in depth in Paper II.

A number of PAH dust emission bands exist within the spectral range of *Spitzer*/IRS, but at low spectral resolution they can be difficult to detect, for example, the 12.7 μm feature which blends with the strong [Ne II] line at 12.81 μm. Therefore, in this paper we focus on the three strongest PAH bands in the usable *IRS* wavelength range: the 6.2, 7.7, and 11.3 μm features. The latter two PAH bands are in fact blends of PAH emission (7.60 and 7.85 μm, 11.23 and 11.33 μm). Other bands that can make a significant contribution are the 8.6 μm band and a blend of PAH emission at 17 μm (17.38 and 17.87 μm), which can be strongly contaminated by H_2 emission.

To fit the data and measure the PAH fluxes we used PAHFIT v1.2,[16] which is an IDL program developed by J. D. T Smith and B. T. Draine for studying PAH features in the mid-IR spectra of the inner regions of local star-forming galaxies (Smith et al. 2007). The PAHFIT model is made up of five components: (1) a starlight continuum, represented as a blackbody with temperature $T = 5000$ K, (2) a featureless thermal dust continuum, represented by an array of eight different blackbody continuum components with temperatures from 35 to 300 K, (3) pure rotational lines of H_2, (4) fine-structure forbidden emission lines, and (5) PAH emission features.

We experimented with, and adapted, the PAHFIT code to check that it functioned appropriately for the samples of powerful radio-loud AGN presented in this paper. For example, we experimented with adding dust components into the model with blackbody temperatures 400 K, 600 K, 1000 K, and 2000 K, in order to account for the potential hotter dust continuum features in the radio galaxy sample spectra. However, PAHFIT fits the data just as well without these extra hot components, which were therefore excluded in the final fit. In addition, when fitting the 10 μm and 18 μm silicate absorption features, we found that the default PAHFIT extinction model did not fit the features well. After some experimentation it was found that the depth of the silicate absorption feature was better fitted

---

[14] For PKS0915−11 (Hydra A), PKS1938−15, 3C305, 3C382, and 3C388 the scaling factor was higher, with values in the range 1.2–3.0. In these cases the objects may not have been exactly centered in the 3.″6 SL slit because of pointing errors, or the mid-IR flux is significantly extended outside the SL slit.

[15] Note [Ar II]λ6.99 μm is not indicated in the plots and may be blended with H_2 S(5)λ6.91 μm.

[16] PAHFIT is made available under the terms of the GNU General Public License.

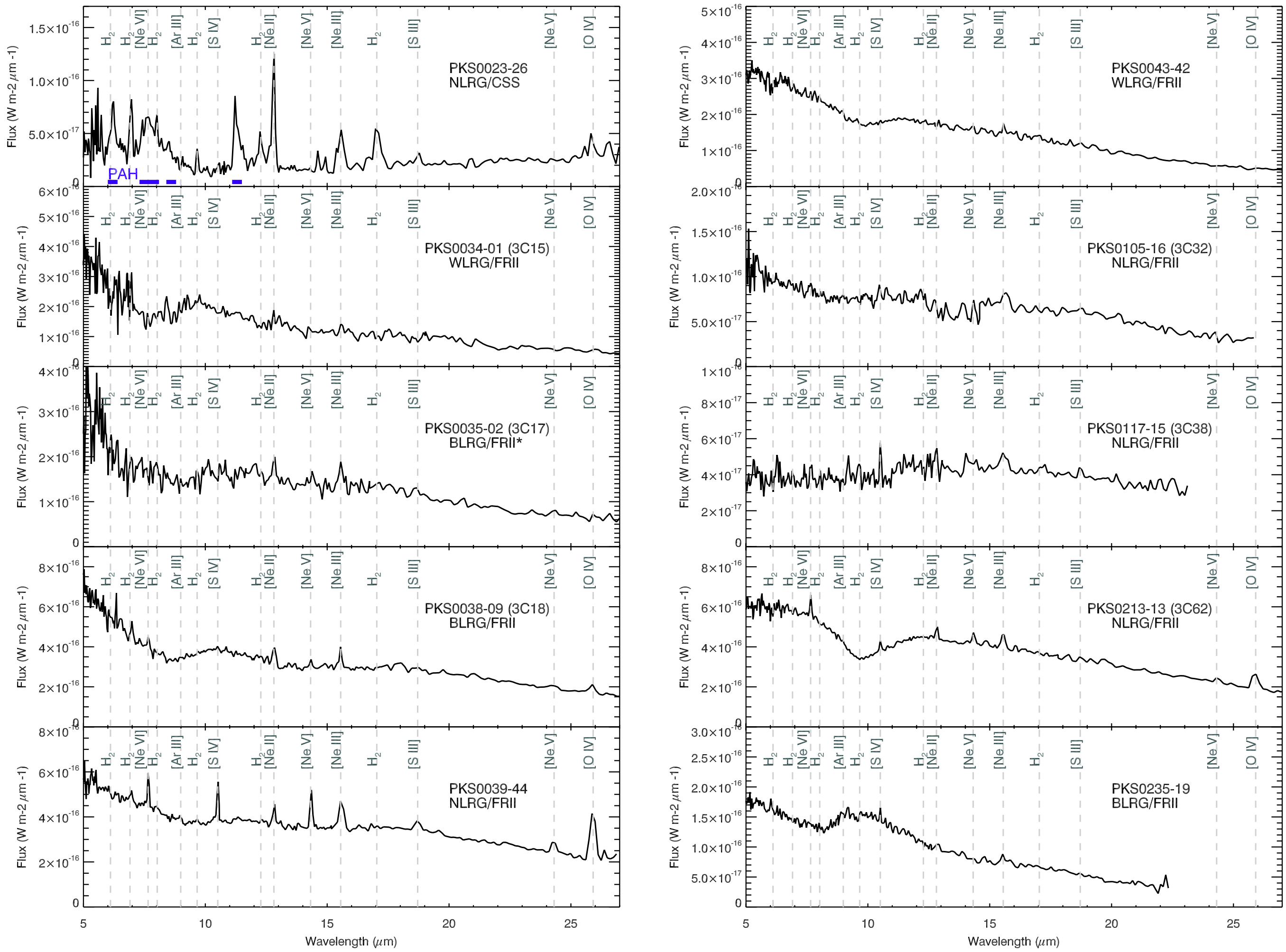

Figure 1. *Spitzer*/IRS spectra for the 2 Jy sample. Common fine-structure and H_2 emission lines are indicated by vertical gray dashed lines. In objects with detected PAH features, the most prominent PAH features are indicated by blue line segments. Note the data for PKS0034−01 and PKS0035−02 were obtained from the *Spitzer* archive. Both potentially suffer from enhanced flux calibration uncertainties at short wavelengths, due to saturation of the peak-up detector (see Section 3 for details).

(A color version of this figure is available in the online journal.)

in models assuming high ratios of 10 to 18 μm opacity. This implies that the 18 μm feature is weak for our samples of powerful radio-loud AGN. Finally, the original PAHFIT model does not include silicate emission because galaxies with such emission were not included in the original PAHFIT sample of Smith et al. (2007). However, for the 2 Jy sample, 10 μm silicate emission is clearly detected at varying strengths in 19% of the observed/detected objects in the 2 Jy and 3CRR samples. Therefore, we made a further adaptation of the PAHFIT program to fit silicate emission as well as absorption, following the method employed in Gallimore et al. (2010).

5. RESULTS

In this section we consider the rate of detection of PAH features in radio galaxies and compare the various star formation diagnostics.

5.1. PAH Detection

It is important to distinguish PAH emission features from fine-structure emission lines, in order to make secure identifications of the PAH bands. Fortunately, the PAH emission bands appear broader than the fine-structure lines, even in low-resolution IRS spectra. The 11.3 μm PAH feature falls in a region of the spectrum without strong fine-structure emission lines, making it an ideal choice for identifying the presence of PAH emission in the radio galaxy samples. In addition, the study of Diamond-Stanic & Rieke (2010) found that the 11.3 μm feature is a more robust indicator of RSFA than the shorter wavelength PAH features in AGN host galaxies. Although it is more susceptible to the effects of silicate absorption and emission than shorter wavelength PAH features such as the 6.2 μm feature, PAHFIT accounts for the effect of silicates when fitting the 11.3 μm PAH emission.

For the objects with good IRS spectra in the combined 2 Jy and 3CRR sample, 9 (16%) objects have PAH features that are clearly detected at high equivalent width (PKS0023−26, PKS0347+05, PKS0915−11, PKS1733−56, PKS2135−20, PKS2314 +03, 3C285, 3C293, 3C305). To show the PAH emission more clearly in these nine objects we present enlargements of their spectra between 5 and 12 μm in Figures 7 and 8 for the 2 Jy and 3CRR samples, respectively.

Using the 11.3 μm feature as a clean identifier, we find eight more objects with low equivalent width (EW) or lower S/N PAH detections (PKS0806−10, PKS1151−34, PKS1814−63, PKS1934−63, 3C33, 3C236, 3C321, 3C326). The detection strategy used to identify PAH emission in these objects was based first on checking that the candidate feature was

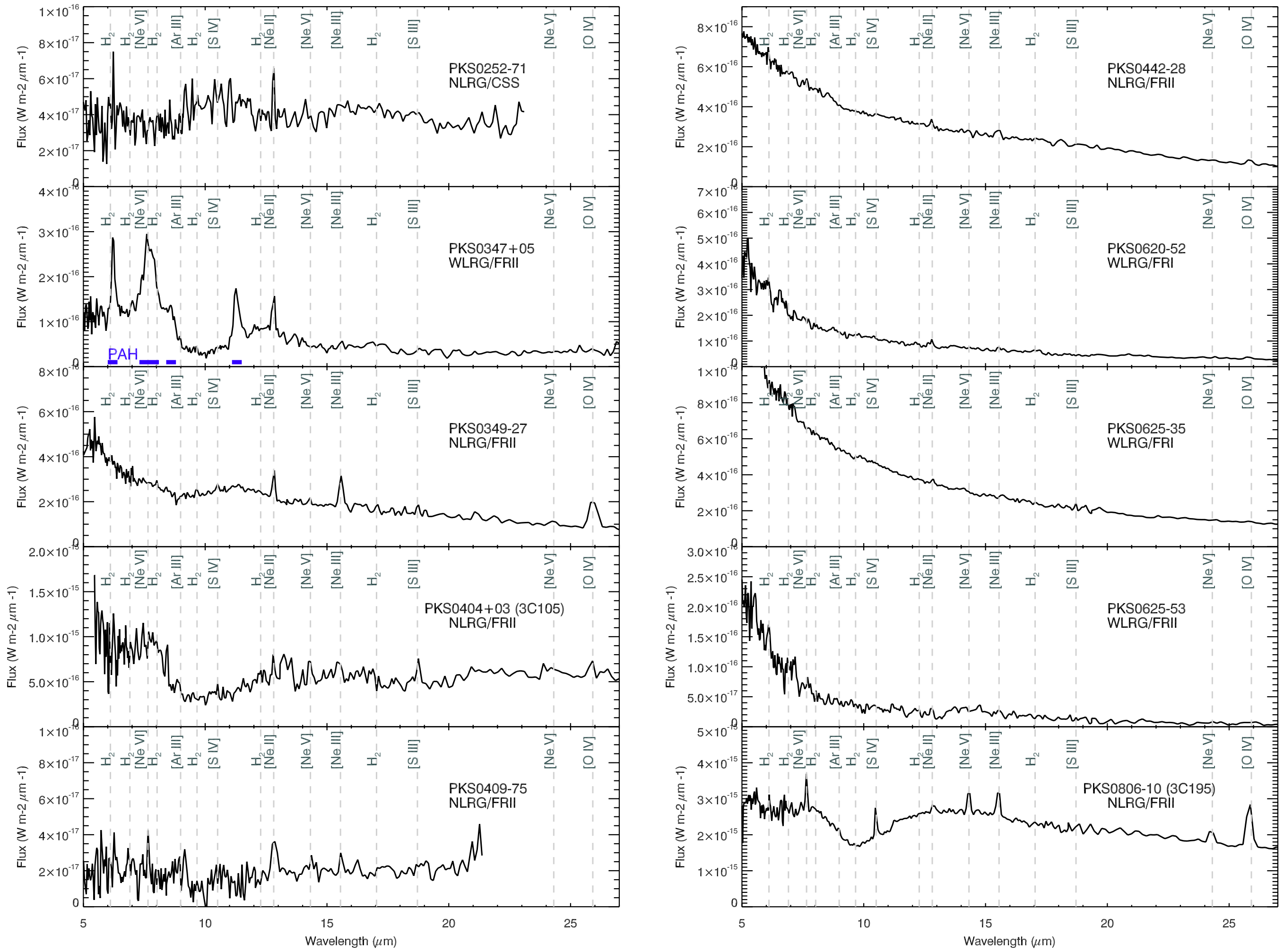

Figure 2. *Spitzer*/IRS spectra for the 2 Jy sample continued. Note the data for PKS0404+03 were taken in mapping mode and were obtained from the *Spitzer* archive.
(A color version of this figure is available in the online journal.)

detected in both nod positions of the IRS spectra (where both were available). Second, we modeled each spectrum with PAHFIT, including or excluding the PAH emission components. After subtracting the PAHFIT model that did not include the PAH components from the spectrum, we were able to analyze the resulting residual spectrum for evidence of PAH emission.

To emphasize these lower level detections we present enlargements of the spectra in Figure 9. Below each spectrum in Figure 9 we plot the residuals from the PAHFIT model, where the solid line represents the residuals from subtracting the spectrum from the PAHFIT model that did not include PAH in the fit, and the dotted line represents residuals of the PAHFIT model that included the PAH features. Four objects (PKS1814−63, PKS1934−61, 3C33, and 3C326) have a prominent 11.3 μm PAH feature fitted well by the PAHFIT model. In addition, low EW PAH features at 7.7 μm appear to be detected. Therefore, we argue that there is good evidence in these four objects for PAH emission.

A further four objects (PKS0806−10, PKS1151−34, 3C236, and 3C321) have lower EW or irregular PAH detections at 11.3 μm. Because the 11.3 μm feature also lies at the red end of the 10 μm silicate absorption feature, potentially the wing of this feature could be mistaken as a low EW signature of PAH. However, for PKS0806−10 and 3C321 the inflection at 11.3 μm is much sharper than expected for the wing of the 10 μm silicate feature; in both objects the feature remains following subtraction of the PAHFIT model that includes silicate absorption but excludes PAH features. Therefore, we regard the detection of PAH features in these two objects as secure.

PKS1151−34 also appears to have a prominent 11.3 μm feature, albeit with an irregular shape. The irregular shape is due to the fact that the feature coincides with the join between the SL and LL parts of the spectrum which hinders a more definitive detection.

Finally, we note that 3C236 also shows a possible 11.3 μm feature detected at low S/N in its low-resolution IRS spectrum (see Figure 9). Although this detection is not secure based on the low-resolution IRS spectrum alone (taken in mapping mode), it has been confirmed with a much higher S/N spectra taken using the high-resolution mode of *Spitzer*/IRS (P. Guillard 2011, private communication).

5.2. *PAH Emission Strength*

PAHFIT uses a Drude profile method to recover the full strength of the PAH dust emission features and blends. Drude profiles are known to recover the flux in PAH features more accurately than methods which estimate the underlying continuum using line segments or spline curve fits, because they better account for the power in the wings of the broad emission

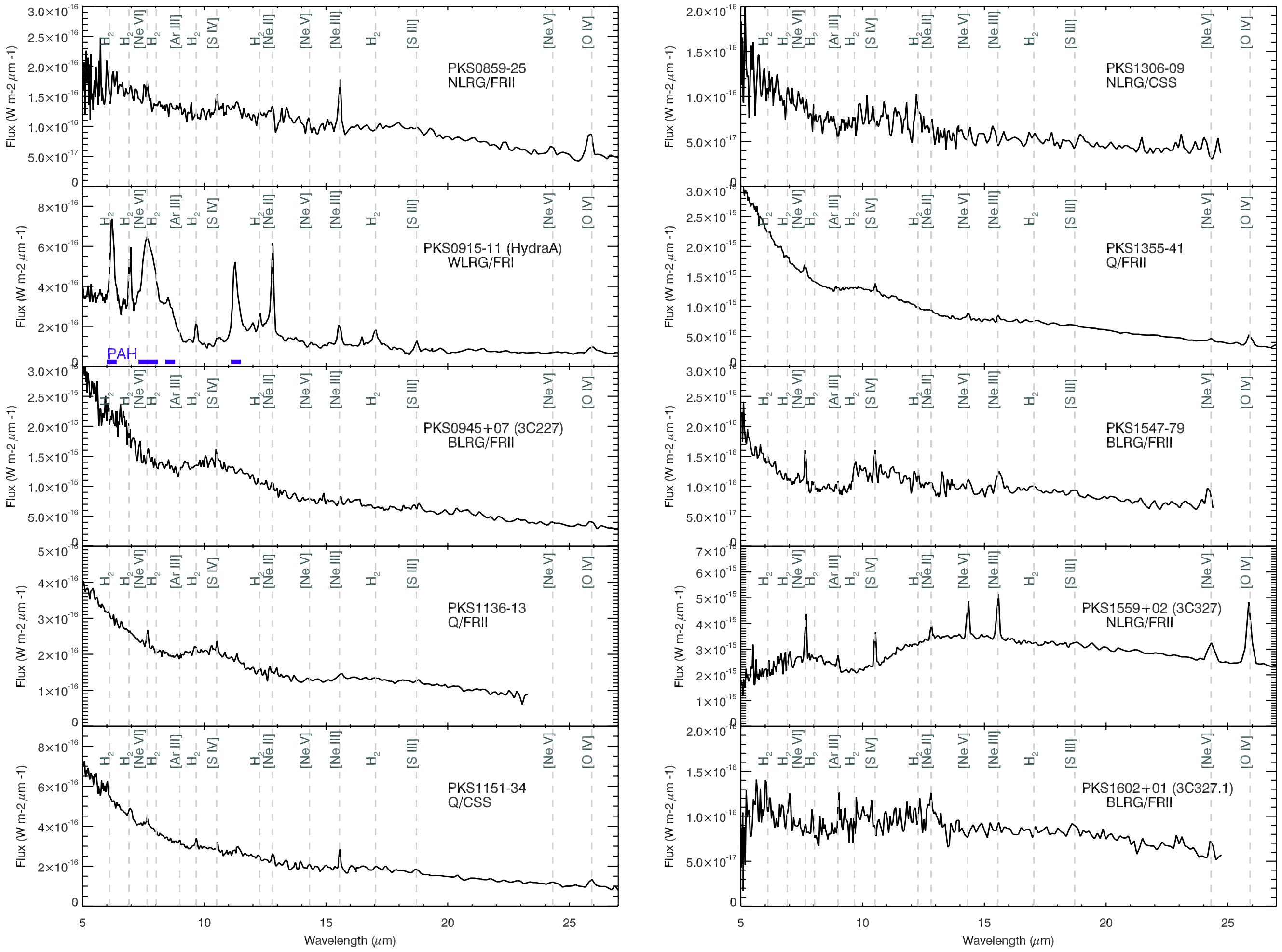

Figure 3. *Spitzer*/IRS spectra for the 2 Jy sample continued. Note the data for PKS0915−11, PKS0945+07, and PKS1602+01 were obtained from the *Spitzer* archive, and the data for PKS0947+07 were taken in mapping mode. Potentially, the spectrum of PKS1602+01 suffers from enhanced flux calibration uncertainties at short wavelengths, due to saturation of the peak-up detector.

(A color version of this figure is available in the online journal.)

profiles. PAHFIT also corrects the PAH fluxes for the corresponding effects of the silicate absorption model fitted to the data. Converting these fluxes into luminosities gives an opportunity to compare the relative strengths of the emission features for all the objects with IRS spectra.

Our PAHFIT model fits the detected 11.3 μm PAH emission features and returns flux values for all the objects in the 2 Jy and 3CRR samples with PAH detections. However, in the case of those objects in which the PAH features are not detected, it is necessary to derive upper limits. To do this in a robust fashion, a scaled IRS spectrum of PKS0915−11 (Hydra A), which is dominated by prominent PAH features, was added to the spectrum of each object without evidence for PAH emission. The scaling factor was varied until a PAH feature at 11.3 μm was just detected in a visual inspection of the combined spectrum. Again the 11.3 μm feature was used, as this is not contaminated by fine-structure lines. Multiplying the measured PAH flux for PKS0915−11 by the scaling factor then gives a robust upper limit on the flux of the PAH. The PAH fluxes and upper limits are presented in Tables 3 and 4.

Using these upper limits we can test whether the objects with detected PAH emission have a unique signature for starbursts, in that the luminosity of the detections is greater than the upper limits, or whether significant PAH emission could exist in all the spectra but may not be detected due to low S/N data. In Figure 10 we plot the 11.3 μm luminosities against the AGN power indicator $L_{[\mathrm{O\,III}]}$. From this figure it is clear that, on average, the PAH luminosities of objects with high EW PAH detections are higher than the majority of PAH upper limits for a comparable $L_{[\mathrm{O\,III}]}$ and AGN power.

The difference in Figure 10 between the PAH detections and the upper limits is clearest for low power AGN, but becomes less clear for higher power AGN. Two factors may contribute to this trend. First, because of limits on the exposure times, some of the more powerful, distant objects have lower S/N spectra than their lower power counterparts at low redshifts, leading to higher upper limit flux values. In this context, not that the group of upper limits around $L_{\mathrm{PAH}} \sim 10^{36}$ W, $L_{[\mathrm{O\,III}]} \sim 10^{35}$ W—comprising PKS0409−75, PKS1306−09, and PKS0252−72—includes some of the highest redshift objects in the 2 Jy sample ($z > 0.5$); these objects have relatively low S/N IRS spectra. Second, the relatively stronger AGN dust continuum emission in the more powerful objects could also lead to higher upper limits for the PAH emission.

The objects with low EW PAH detections are also marked in Figure 10. In general, they occupy the same region of the plot as the upper limits, but tend to lower PAH luminosities compared to the higher EW PAH detections.

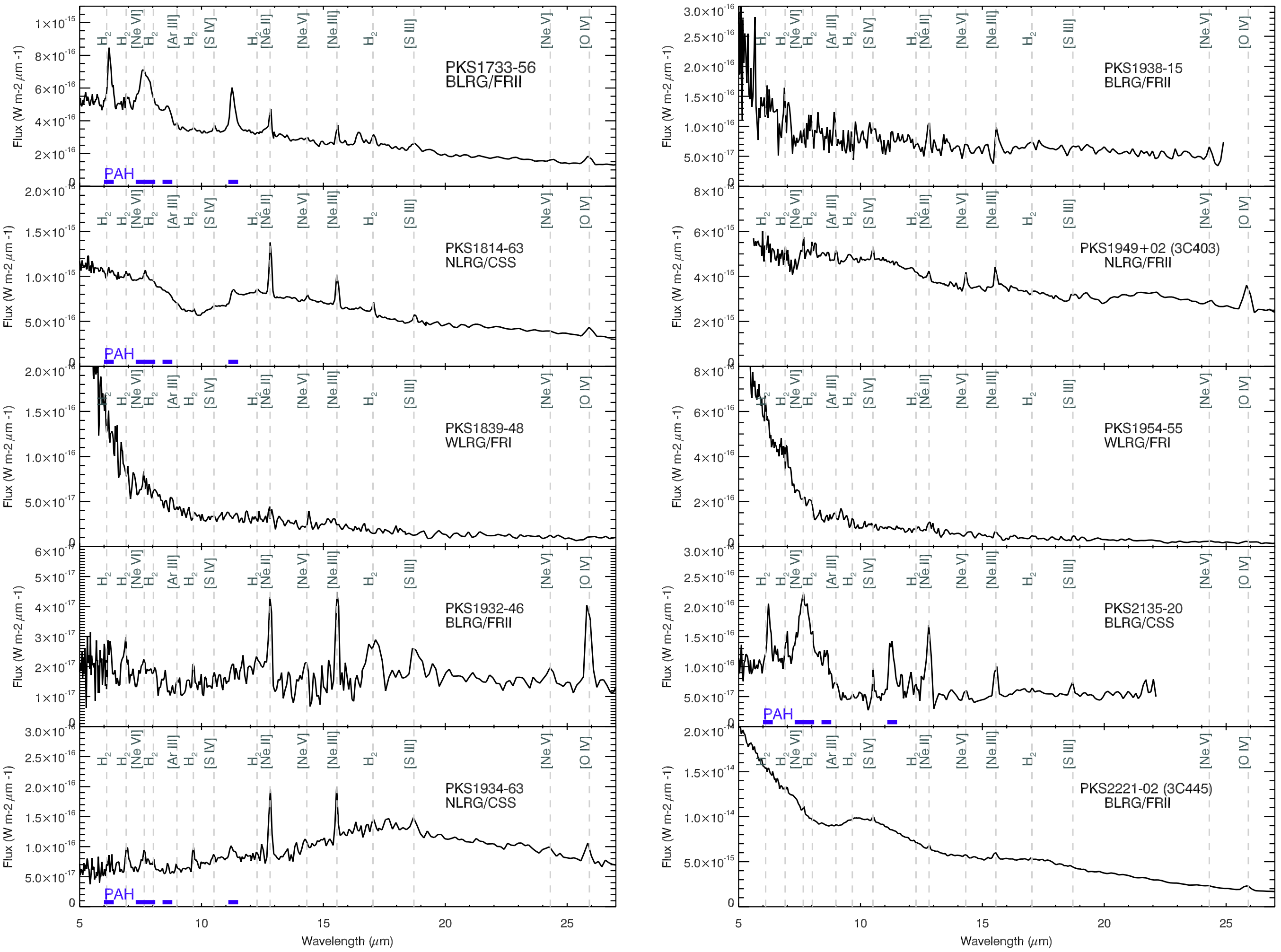

Figure 4. *Spitzer*/IRS spectra for the 2 Jy sample continued. Note that the data for PKS1949+02 (mapping mode) and PKS2221−02 were obtained from the *Spitzer* archive.

(A color version of this figure is available in the online journal.)

From these data alone it is impossible to entirely rule out RSFA activity, at some level, in the objects with PAH upper limits. However, the position of the upper limits for lower luminosity AGN argues against powerful starburst activity in these objects.

By combining the spectra that have no evidence for PAH features, it is possible to create a spectrum with high signal to noise to investigate the possibility of low level PAH emission in the objects without individual detections. We present median spectra for the objects without PAH detections in the combined 2 Jy and 3CRR sample in Figure 11. These median spectra were created by re-sampling the spectral data in wavelength bins and normalizing all the spectra to have the same flux at 20 μm. While the median spectrum of the PAH identified objects shows the characteristic PAH emission dominating the spectrum, the median spectrum for objects in which we have not individually identified PAH shows no evidence for PAH features.

Also in Figure 11 we present median spectra for objects without individually identified PAH features divided into BLRG and NLRG. We can use these median spectra to test the idea that a stronger AGN continuum in BLRG may mask low level PAH emission, which in turn may be more easily detected in NLRG. The test is again negative, revealing no evidence for PAH emission in the NLRG.

5.3. Comparison with Optical Star Formation Indicators

Careful spectral synthesis modeling of deep optical spectra for the 2 Jy (Tadhunter et al. 2002; Wills et al. 2004, 2008; Holt et al. 2007; Tadhunter et al. 2012, in preparation) and 3CRR (see Dicken et al. 2010 and references therein) samples has allowed identification of objects with evidence for RSFA at optical wavelengths.

Considering the objects with high EW PAH detections that also have deep optical spectra available, it is notable that *all* eight of these objects show evidence of young stellar populations in their optical spectra. In addition, we have identified RSFA through PAH detection in one object (PKS1733−56) for which the contamination by direct AGN emission components precluded the identification of any young stellar populations at optical wavelengths.

Out of the 13 objects with good optical evidence for RSFA and IRS spectra, only 3 objects show no evidence for PAH features (PKS0409−75, PKS0620−52, PKS1932−46). The relatively low S/N of the spectra in the region of the 11.3 μm PAH feature for these three objects (S/N = 2, 13, and 4, respectively, compared with the sample average of 24) could help to explain why no PAH emission is detected.

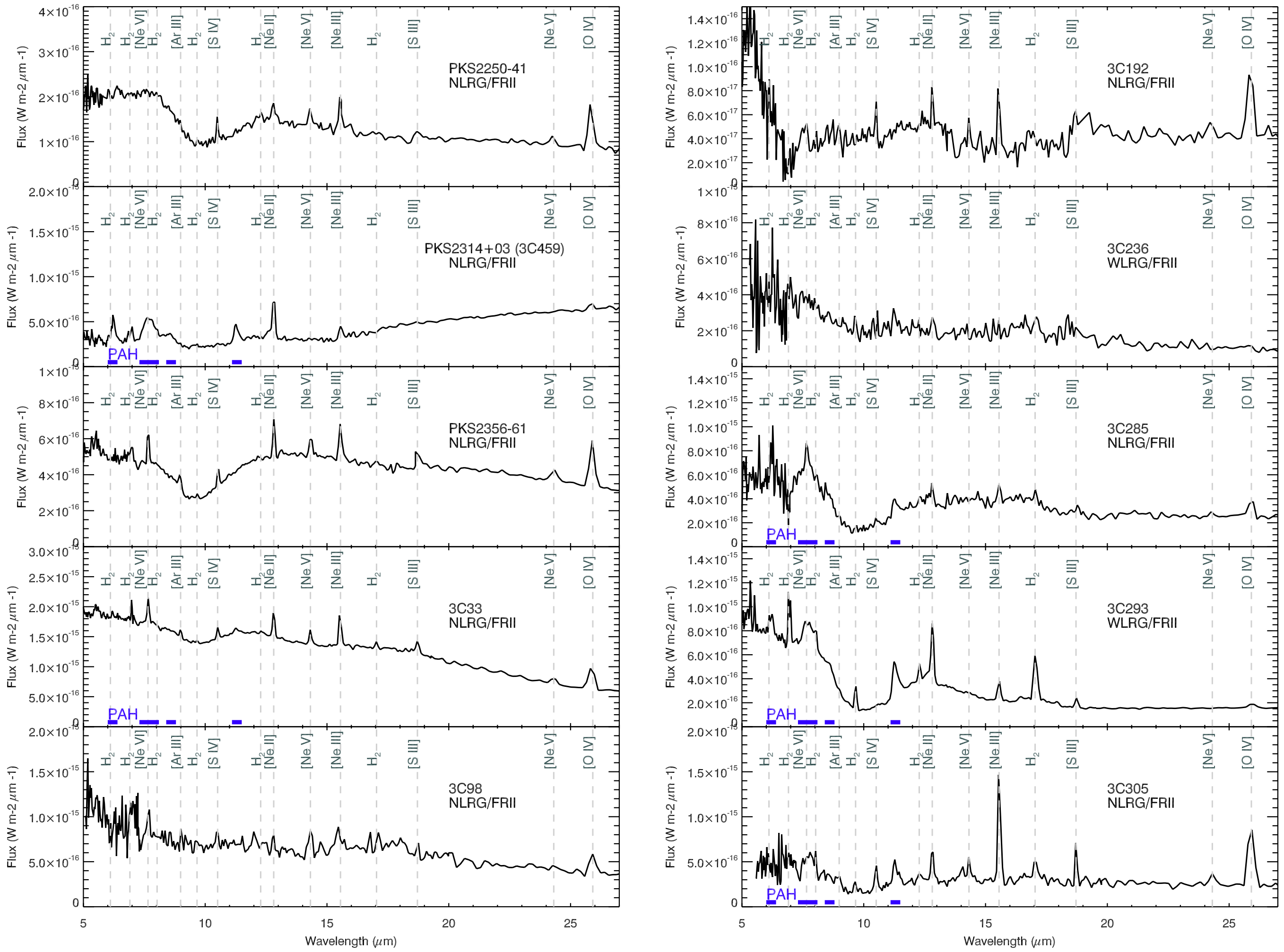

Figure 5. *Spitzer*/IRS spectra for the 2 Jy and 3CRR sample objects. All the 3CRR IRS data were obtained from the *Spitzer* archive. The data for 3C98, 3C236, 3C277.3, 3C285, and 3C305 were taken in mapping mode and were obtained from the *Spitzer* archive.

(A color version of this figure is available in the online journal.)

Overall the optical and PAH evidence for RSFA correlates well. The correlation is unlikely to be perfect since the two star formation indicators do not necessarily sample star formation activity on the same spatial scales, or at the same evolutionary stages of the starbursts. For example, in a significant subset of the radio galaxies with optically identified young stellar populations we are detecting post-starburst stellar populations that are observed a significant period (∼0.1–2 Gyr) after the peak of merger-induced star formation activity (Tadhunter et al. 2005, 2011). In addition, identification of RSFA at optical wavelengths is not possible in some objects due to a strong AGN continuum that masks these signatures. Equally, PAH identification may be hindered by low S/N spectra and/or calibration errors such as noted for 3C15 (see Section 3).

Combining the objects that have high EW PAH detections (9) and the objects that have clear optically identified RSFA (13) makes a total of 14 objects (22%) with strong evidence for RSFA in the combined 2 Jy and 3CRR sample.

Next we consider the six objects with low EW PAH detections that also have deep optical spectra available. Only two of these objects—3C236, 3C321—have evidence for RSFA at optical wavelengths. The low EW PAH detections in the remaining four objects—PKS0806−10, PKS1934−63, 3C33, and 3C326—may represent a low level of star formation that could not be detected at optical wavelengths. However, it is also important to consider that the low EW PAH emission may originate from ISM diffuse PAH emission rather than be associated with RSFA (Kaneda et al. 2008), particularly for objects with low AGN continuum strength such as 3C326.

Finally, we return to the question posed in the introduction of whether there is a substantial population of radio galaxies in which the RSFA is missed at optical wavelengths due to dust obscuration. We find that, of the 38 objects that have good optical spectroscopic information and show no sign of RSFA in their optical spectra, only the 4 objects (11%) discussed above—PKS0806−10, PKS1934−63, 3C33, and 3C326—have PAH features detected in their mid-IR spectra; and these are all low EW detections. Therefore, the incidence of objects in our samples that have obscured RSFA that is not already detected at optical wavelengths is relatively minor.

5.4. Mid- to Far-IR Color

A common method for identifying star formation activity involves using the MFIR color. Both the 2 Jy and 3CRR samples have complete *Spitzer* MIPS data which can be used to investigate the F(70)/F(24) flux ratio (D09; D10). Empirically,

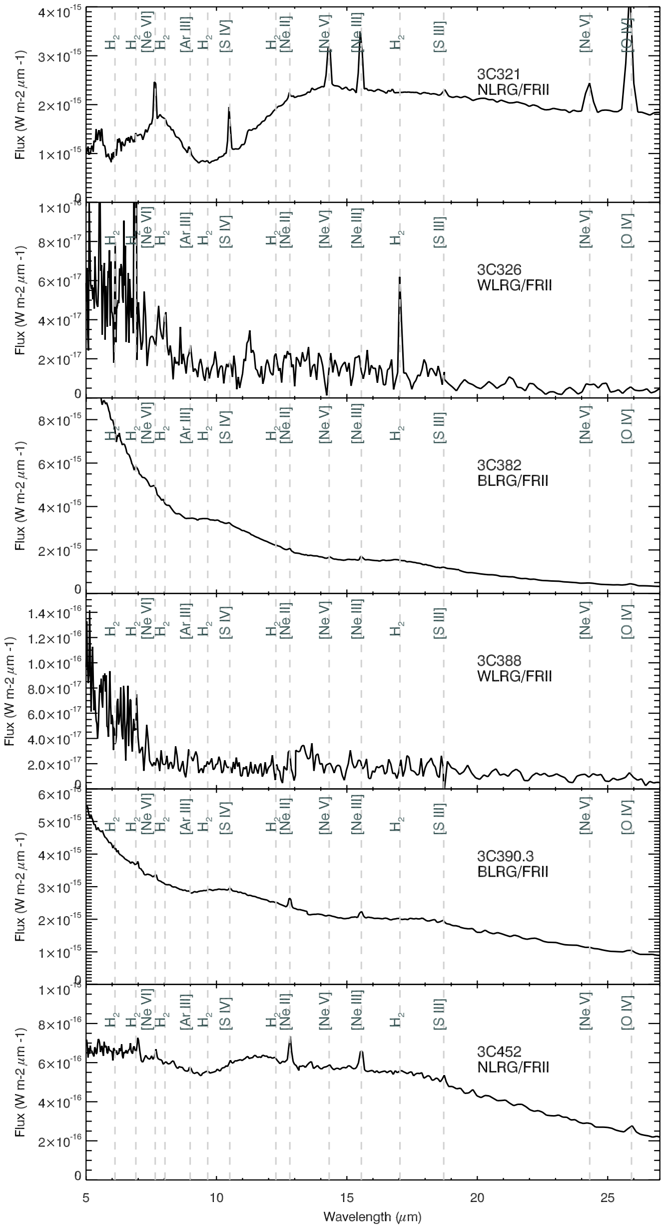

Figure 6. *Spitzer*/IRS spectra of the 3CRR sample continued.

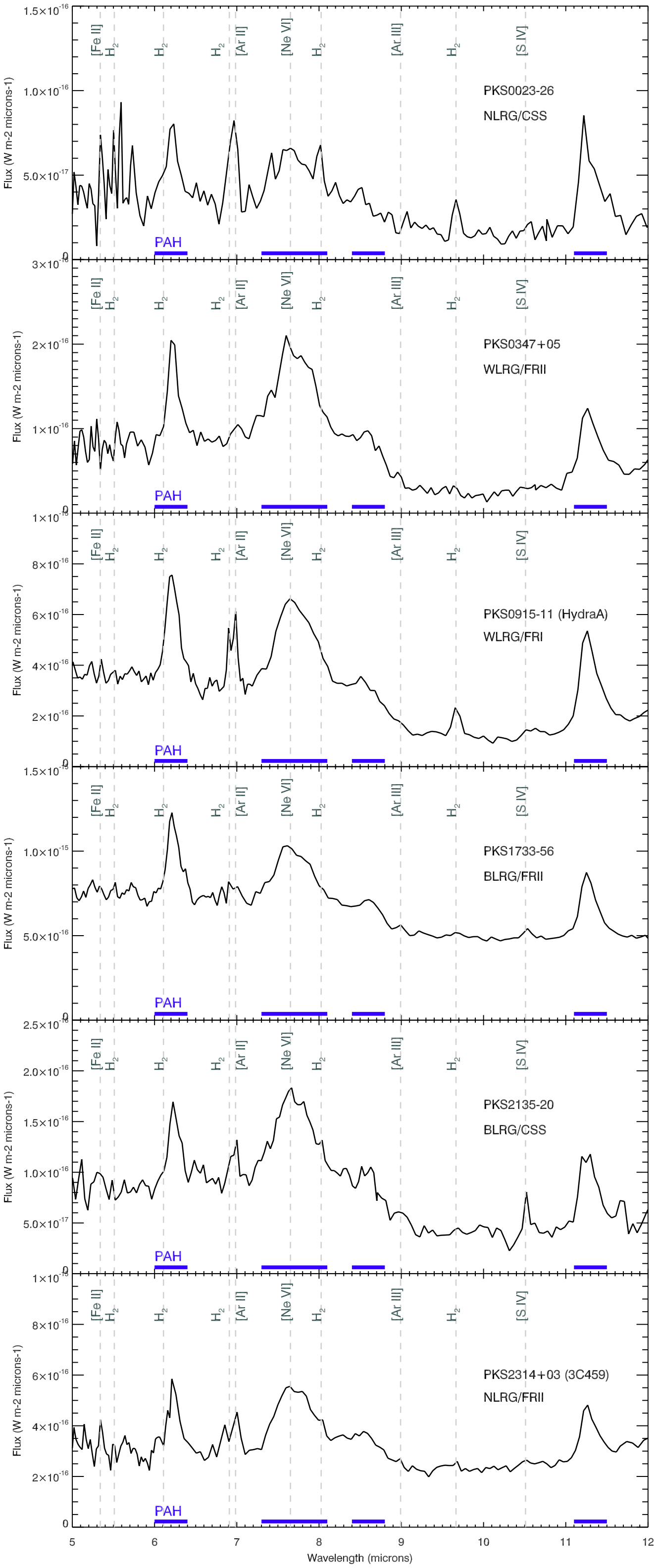

Figure 7. Magnified IRS spectra focusing on the 5–12 μm band of IRS to emphasize the dominant PAH bands at 6.2, 7.7, and 11.3 μm. The six objects in the 2 Jy sample with visually identifiable PAH emission are shown.

(A color version of this figure is available in the online journal.)

starburst galaxies are known to be associated with cool MFIR colors, as expected in the case of illumination of extended dust structures by spatially distributed star-forming regions. Unlike PAH emission, the MFIR color diagnostic is not a clean identifier of RSFA, because the far-IR emitting dust can be heated by AGN and/or young stellar populations. However, in our previous work (D09; D10) we have shown that optically identified RSFA objects do tend to have cooler MFIR colors. With the addition of the more complete PAH identified RSFA objects from the 2 Jy and 3CRR samples, we can thoroughly test the MFIR color star formation diagnostic for radio-loud AGN.

Figure 12 presents a histogram of the MFIR colors for the 2 Jy and 3CRR samples, with the RSFA objects indicated. It is immediately clear that all but one of the 11 objects with F(70)/F(24) $>$ 5 show evidence for RSFA on the basis of optical and/or PAH data, whereas the majority of objects lacking such evidence cluster around MFIR colors of F(70)/F(24) $\approx$ 0.5–2.5. However, there is a mix of objects in the range 2.5 $<$ F(70)/F(24) $<$ 5, which may represent a MFIR color transition region between AGN-dominated and RSFA-dominated objects. Objects in this transition region with F(70)/F(24) $\approx$ 4.5 include PKS0349−27 and PKS1306−09. We note that these latter two

Table 3
The 2 Jy Sample—PAH Flux Data

PKS Name	Other	z	Opt.	Rad.	$S_{11.3}$ (W m^{-2})	70/24
0023−26		0.322	NLRG	CSS	$(3.4 \pm 0.1) \times 10^{-17}$	12.2 ± 2.1
0034−01	3C15	0.073	WLRG	FRII	<6.6E-18	2.4 ± 0.3
0035−02	3C17	0.220	BLRG	(FRII)	<1.3E-17	1.9 ± 0.4
0038 + 09	3C18	0.188	BLRG	FRII	<6.6E-18	1.2 ± 0.2
0039−44		0.346	NLRG	FRII	<2.0E-17	2.1 ± 0.1
0043−42		0.116	WLRG	FRII	<6.6E-18	0.9 ± 0.3
0105−16	3C32	0.400	NLRG	FRII	<2.0E-17	<1
0117−15	3C38	0.565	NLRG	FRII	<6.6E-18	3.3 ± 0.3
0213−13	3C62	0.147	NLRG	FRII	<6.6E-18	0.9 ± 0.1
0235−19	OD-159	0.620	BLRG	FRII	<1.3E-17	1.3 ± 0.2
0252−71		0.566	NLRG	CSS	<6.6E-18	<3
0347 + 05		0.339	WLRG	FRII	$(8.9 \pm 0.1) \times 10^{-17}$	8.8 ± 1.3
0349−27		0.066	NLRG	FRII	<6.6E-18	4.8 ± 0.2
0404 + 03	3C105	0.089	NLRG	FRII	<2.0E-17	2.3 ± 0.1
0409−75		0.693	NLRG	FRII	<9.9E-18	7.3 ± 1.9
0442−28		0.147	NLRG	FRII	<6.6E-18	1.4 ± 0.2
0620−52		0.051	WLRG	FRI	<6.6E-18	10.5 ± 0.4
0625−35	OH-342	0.055	WLRG/BLLac	FRI	<6.6E-18	1.8 ± 0.1
0625−53		0.054	WLRG	FRII	<6.6E-18	<6
0806−10	3C195	0.110	NLRG	FRII	$(1.8 \pm 1.5) \times 10^{-17}$	1.90 ± 0.01
0859−25		0.305	NLRG	FRII	<6.6E-18	0.9 ± 0.3
0915−11	Hydra A	0.054	WLRG	FRI	$(1.1 \pm 0.1) \times 10^{-16}$	12.9 ± 0.6
0945 + 07	3C227	0.086	BLRG	FRII	<4.0E-17	0.4 ± 0.1
1136−13		0.554	Q	FRII	<2.0E-17	1.7 ± 0.2
1151−34		0.258	Q	CSS	$(3.0 \pm 0.1) \times 10^{-17}$	3.2 ± 0.2
1306−09		0.464	NLRG	CSS	<6.6E-18	4.7 ± 0.5
1355−41		0.313	Q	FRII	<1.3E-17	1.25 ± 0.04
1547−79		0.483	BLRG	FRII	<1.3E-17	2.4 ± 0.2
1559 + 02	3C327	0.104	NLRG	FRII	<2.6E-17	1.94 ± 0.02
1602 + 01	3C327.1	0.462	BLRG	FRII	<1.3E-17	1.6 ± 0.3
1648 + 05	Herc A	0.154	WLRG	FRI	...	<9
1733−56		0.098	BLRG	FRII	$(1.3 \pm 0.1) \times 10^{-16}$	5.2 ± 0.1
1814−63		0.063	NLRG	CSS	$(8.2 \pm 0.5) \times 10^{-17}$	2.35 ± 0.04
1839−48		0.112	WLRG	FRI	<6.6E-18	3.5 ± 0.9
1932−46		0.231	BLRG	FRII	<6.6E-18	7.1 ± 0.7
1934−63		0.183	NLRG	GPS	$(1.3 \pm 0.1) \times 10^{-17}$	1.1 ± 0.1
1938−15		0.452	BLRG	FRII	<1.3E-17	2.9 ± 0.6
1949 + 02	3C403	0.059	NLRG	FRII	<4.0E-17	1.80 ± 0.02
1954−55		0.060	WLRG	FRI	<6.6E-18	3.3 ± 1.1
2135−14		0.200	Q	FRII	...	1.08 ± 0.05
2135−20	OX-258	0.635	BLRG	CSS	$(1.1 \pm 0.1) \times 10^{-16}$	8.7 ± 1.0
2211−17	3C444	0.153	WLRG	FRII	...	<18
2221−02	3C445	0.057	BLRG	FRII	<6.6E-17	0.80 ± 0.02
2250−41		0.310	NLRG	FRII	<2.6E-18	1.9 ± 0.2
2314 + 03	3C459	0.220	NLRG	FRII	$(1.1 \pm 0.1) \times 10^{-16}$	10.3 ± 0.1
2356−61		0.096	NLRG	FRII	<1.3E-17	1.8 ± 0.1

Notes. Table presenting PHA fluxes measured using the PAHFIT program for all 2 Jy objects with useful *IRS* data. Uncertainties are derived from the PAHFIT model fit. See Table 6 for ratios of 11.3/6.2 μm and 11.3/7.7 μm fluxes. PKS0347+05 had been classified in our previous work as a BLRG (T07; D08; D09), however, we have since determined that the broad-line component comes from a companion galaxy and not the radio galaxy, therefore it is now classified as a WLRG. The uncertainties on the 70/24 ratios do not include the instrumental calibration uncertainties (4% and 10% for 24 microns and 70 microns respectively).

objects do not have the high-quality spectra required to detect the signatures of RSFA at optical wavelengths. It is also noteworthy that PKS1306−09 is a CSS object that shows a strong far-IR excess, in the sense that it falls well above the $L_{70\,\mu\mathrm{m}}$ versus $L_{[\mathrm{O\,III}]}$ correlation (see Section 6.4).

All the objects with either high EW PAH and/or optical evidence for RSFA (highlighted in dark blue in Figure 12) show relatively cool MFIR colors with $70\,\mu\mathrm{m}/24\,\mu\mathrm{m} > 3$. Therefore, this study finds that MFIR color is an excellent indicator of starburst activity in radio galaxies. This is consistent with the results found by Brandl et al. (2006) for AGN using the F(15)/F(30) ratio, and by Veilleux et al. (2009) using the F(60)/F(25) ratio for at large sample of ultraluminous infrared galaxies (ULIRGs) with varying AGN contribution.

Of the eight objects with low EW PAH detections, five have been identified in Figure 12, while a further two objects (3C236 and 3C321) are already highlighted in this figure as optical RSFA objects (dark blue) with F(70)/F(24) = 3.7 and 3.4, respectively. The eighth low EW PAH object (3C326) is not included in this figure because it has an upper limit on F(70)/F(24). The figure shows that the MFIR colors of the low EW PAH objects are similar to those of objects lacking PAH

Table 4
The 3CRR Sample—PAH Flux Data

Name	z	Opt.	Rad.	$S_{11.3}$ (W m^{-2})	70/24
3C33	0.060	NLRG	FRII	$(8.9 \pm 0.6) \times 10^{-17}$	1.46 ± 0.03
3C35	0.067	WLRG	FRII	···	21.0 ± 8.6
3C98	0.030	NLRG	FRII	<1.3E-17	0.8 ± 0.1
DA240	0.036	WLRG	FRII	···	8.3 ± 1.5
3C192	0.060	NLRG	FRII	<2.6E-17	2.4 ± 1.1
4C73.08	0.058	NLRG	FRII	···	0.5 ± 0.1
3C236	0.101	WLRG	FRII	$(5.4 \pm 0.1) \times 10^{-17}$	3.7 ± 0.3
3C277.3	0.085	WLRG	FRI/FRII	···	2.1 ± 0.4
3C285	0.079	NLRG	FRII	$(1.3 \pm 0.1) \times 10^{-16}$	4.3 ± 0.1
3C293	0.045	WLRG	FRI/FRII	$(2.3 \pm 0.1) \times 10^{-16}$	9.7 ± 0.2
3C305	0.042	NLRG	FRII/CSS	$(1.4 \pm 0.3) \times 10^{-16}$	7.1 ± 0.1
3C321	0.096	NLRG	FRII	$(1.5 \pm 0.1) \times 10^{-17}$	3.40 ± 0.02
3C326	0.090	NLRG	FRII	$(1.1 \pm 0.1) \times 10^{-17}$	<13
3C382	0.058	BLRG	FRII	<1.3E-17	0.57 ± 0.04
3C388	0.092	WLRG	FRII	<6.6E-18	<4
3C390.3	0.056	BLRG	FRII	<2.6E-17	0.75 ± 0.01
3C452	0.081	NLRG	FRII	<6.6E-18	1.0 ± 0.1

Notes. Table presenting PAH fluxes measured using the PAHFIT program for all 3CRR objects with useful *IRS* data. Note that 3C403 and 3C445 overlap between the two samples; see Table 3 for PAH data for these latter objects.

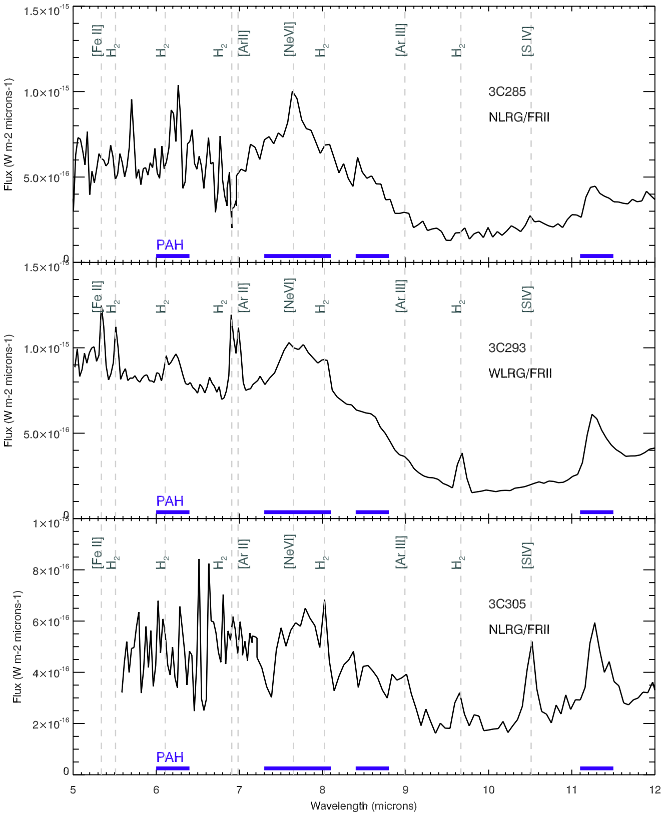

Figure 8. Magnified IRS spectra continued. The three objects in the 3CRR sample with visually identifiable PAH emission are shown. Note that 3C285 and 3C305 were observed in mapping mode and therefore suffer from lower S/N.

(A color version of this figure is available in the online journal.)

detections. This result is not surprising assuming that the low EW PAH detections represent a low level of star formation activity or indeed if the PAH has a diffuse ISM emission origin rather than a stellar origin as mentioned above in Section 5.3. It is notable that the two low EW PAH objects with the coolest colors, 3C236 and 3C321, mentioned above, also have optical RSFA detections.

It is also important to consider the possibility of RSFA in the three objects from the 2 Jy sample and the four objects from the 3CRR sample that were not observed/detected with *Spitzer*/IRS. None of these objects have optical evidence for RSFA. However, two of the closest objects ($z \approx 0.03$) 3C35 and DA240 have cool MFIR colors (=21.0 ± 8.6 and 8.3 ± 1.5, respectively). We have excluded 3C35 from this analysis because its measured F(70)/F(24) has a large uncertainty. DA240 is the only object with cool MFIR colors F(70)/F(24) >5 without clear optical or PAH identification of RSFA. On the other hand, this object does show evidence for RSFA in the form of a far-IR excess (see Section 5.5 and Table 5).

5.5. Far-IR Excess

Our previous work has shown that the objects with optically identified RSFA have enhanced emission at far-IR wavelengths compared to the majority of the sample objects (T07; D09; D10). Several objects in these previous studies also showed apparent enhancements in their far-IR emission, but optical identification of RSFA was not possible. We are now able to revisit this investigation with the benefit of the IRS data and PAH detections to see if our previous result holds with the new, more complete, RSFA identifications.

In Figure 13, we plot $L_{24\,\mu\mathrm{m}}$ and $L_{70\,\mu\mathrm{m}}$ against $L_{[\mathrm{O\,III}]}$ for the 2 Jy and 3CRR samples. As discussed in Section 1, $L_{[\mathrm{O\,III}]}$ is a good indicator of the intrinsic power of the AGN. Consequently, we interpret the similar slopes of the correlations[17] between $L_{24\,\mu\mathrm{m}}$, $L_{70\,\mu\mathrm{m}}$, and $L_{[\mathrm{O\,III}]}$ seen in Figure 13 as direct evidence for AGN illumination as the dominant heating mechanism of the thermal MFIR emitting dust (D09; D10). Considering the spectral diversity seen in the IRS data presented in this paper, the correlation between the mid-IR luminosity ($L_{24\,\mu\mathrm{m}}$) and $L_{[\mathrm{O\,III}]}$ is striking.

Following the method of our previous investigations we have marked with blue stars in Figure 13 those objects with high EW PAH detections and/or optical evidence for RSFA in the 2 Jy and 3CRR samples. Consistent with our previous studies, there is little difference between the distributions of RSFA and non-RSFA objects in the $L_{24\,\mu\mathrm{m}}$ versus $L_{[\mathrm{O\,III}]}$ plot (Figure 13(a)). In contrast, Figure 13(b) clearly shows that all but one (PKS1932−46)[18] of the 14 objects with optical and/or PAH evidence for RSFA in the 2 Jy and 3CRR samples lie above the $L_{70\,\mu\mathrm{m}}$ versus $L_{[\mathrm{O\,III}]}$ correlation defined by the regression line fitted to the no-RSFA objects.

This boosting of the objects with evidence for RSFA above the correlation between $L_{70\,\mu\mathrm{m}}$ and $L_{[\mathrm{O\,III}]}$ in Figure 13—by more than an order of magnitude in some cases—provides strong evidence for enhancement of the thermal far-IR emission by RSFA. Conducting a one-dimensional Kolmogorov–Smirnov two-sample test on the combined sample, comparing the vertical displacements from our fitted regression line in the $L_{70\,\mu\mathrm{m}}$ versus

---

[17] Spearman partial rank correlation tests presented in D10 show that the correlations are intrinsic and do not arise because $L_{[\mathrm{O\,III}]}$ and L_{MFIR} are independently correlated with redshift. The null hypothesis that the variables are unrelated is still rejected at the >99.5% level of significance.

[18] This object is discussed in detail in D10. Among the objects with optically identified RSFA, this object has the weakest evidence for RSFA in its near-nuclear regions, with the evidence confined to the detection of H II region-like emission line ratios in the extended halo of the galaxy (Villar-Martín et al. 2005).

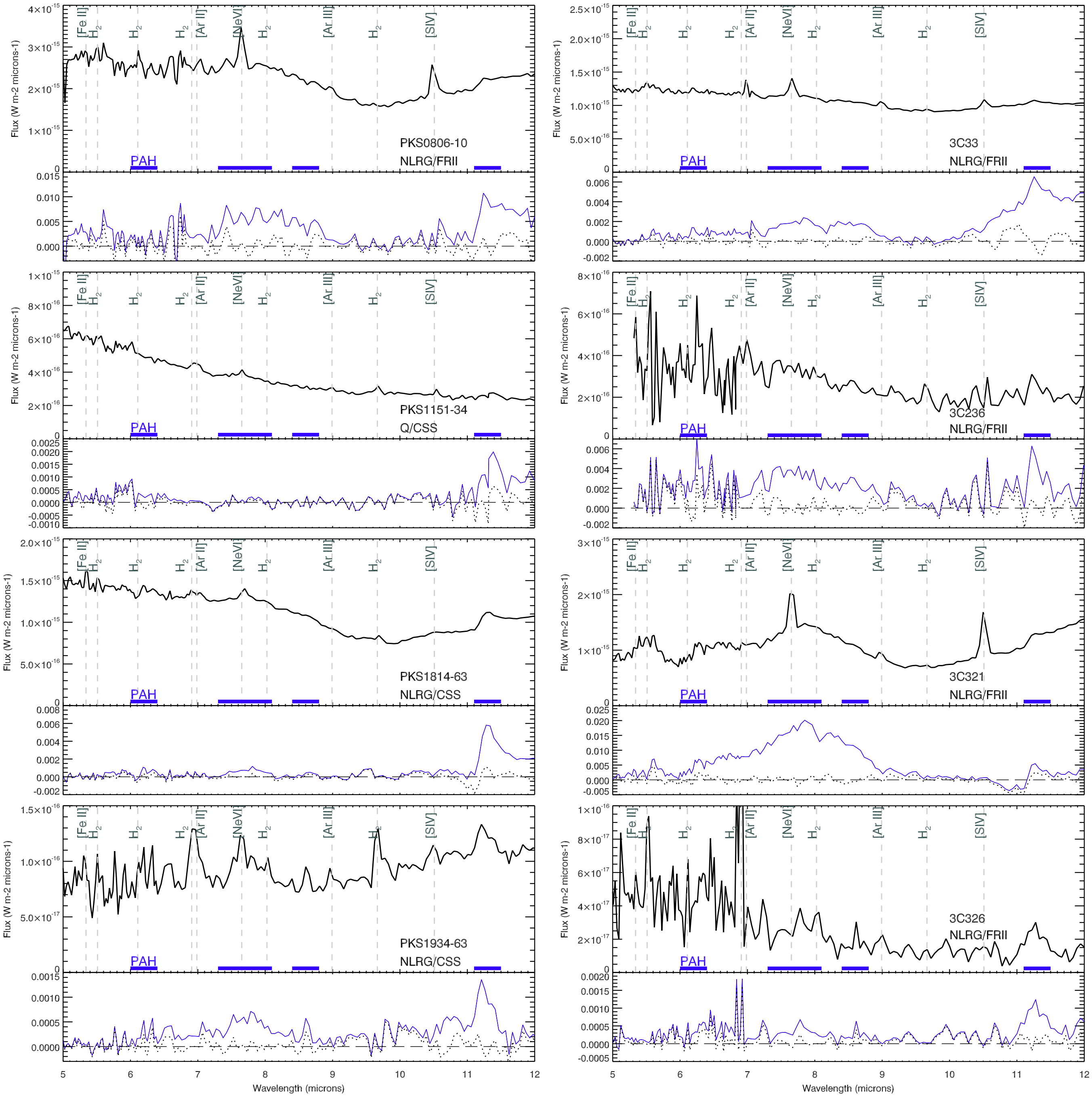

Figure 9. Magnified IRS spectra focusing on the 5–12 μm band presenting the objects deemed to have low EW PAH. Below each spectrum are plotted the residuals from the PAHFIT fit, the solid line representing the PAHFIT fit without PAH and the dotted line representing a fit with PAH component. See Section 5.1 for more details.

(A color version of this figure is available in the online journal.)

$L_{[\mathrm{O\,III}]}$ plot, we find that we can reject the null hypothesis that the objects with and without independent optical/PAH evidence for RSFA are drawn from the same parent population at a better than 0.01% level of significance. Note that, in conducting this analysis, we included upper limits on $L_{70\,\mu\mathrm{m}}$ and $L_{[\mathrm{O\,III}]}$ as actual measurements.

To take into account the upper limits in a more rigorous manner, we also investigated the differences in the distributions of $L_{70\,\mu\mathrm{m}}$ and $L_{[\mathrm{O\,III}]}$ including the upper limits, using survival statistics in the ASURV package (Isobe et al. 1986; Lavalley et al. 1992) as implemented in IRAF. Specifically, the "twosampt" task, which computes several nonparametric two-sample tests for comparing two or more censored data sets, was used. These tests revealed that the 70 μm flux was significantly different in the starburst versus the non-starburst populations. For instance, the Gehan's Generalized Wilcoxon test estimated that the probability (p) that the two sets of censored data belonged to the same population was 0.023 (test statistic = 2.268) while the Logrank test estimates $p = 0.013$ (test statistic = 2.483). On the other hand, the [O III] flux was not significantly different between the two populations: the Gehan's Generalized Wilcoxon test gave a test statistic of 0.531 and

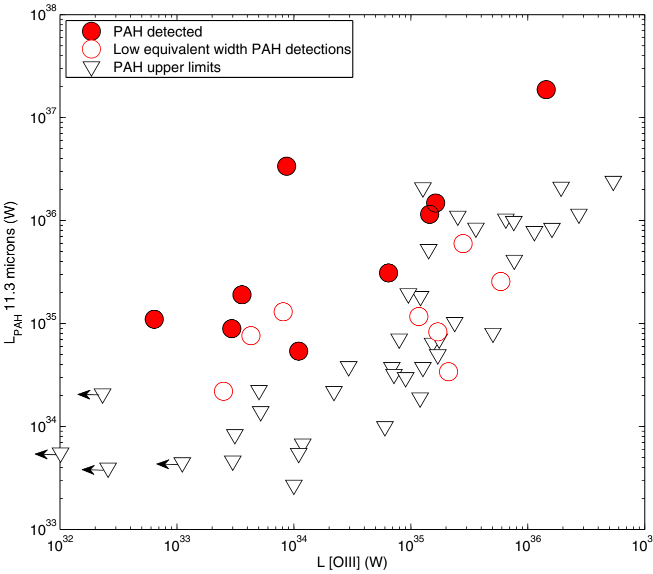

Figure 10. Plot of $L_{\mathrm{PAH}11.3}$ vs. $L_{[\mathrm{O\,III}]}$.

(A color version of this figure is available in the online journal.)

$p = 0.595$, while the Logrank test gave a test statistic of 0.123 and $p = 0.902$.

We have also plotted the objects with low EW PAH detections on Figure 13. Many of the low EW PAH objects fall above the $L_{70\,\mu\mathrm{m}}$ versus $L_{[\mathrm{O\,III}]}$ correlation, but the result is not as clear-cut as it is for the high EW PAH objects. It is noteworthy that the low EW PAH object furthest above the fitted regression line in the $L_{70\,\mu\mathrm{m}}$ versus $L_{[\mathrm{O\,III}]}$ correlation—3C321—has the coolest MFIR colors out of all the low EW PAH objects (F(70)/F(24) = 3.4) and also optical identification of RSFA. This object is indicated with a filled star in Figure 13.

In terms of whether the far-IR excess alone is a good indicator of RSFA, we find that all 13 of the objects that fall more than 0.5 dex (factor of three) above the $L_{70\,\mu\mathrm{m}}$ and $L_{[\mathrm{O\,III}]}$ regression line also show evidence for significant RSFA based on at least two of the other indicators. We conclude that far-IR excess is as useful an indicator of RSFA in radio galaxies as MFIR color.

6. DISCUSSION

6.1. *Star Formation Activity in Radio-loud AGN*

Our multi-wavelength data set allows us to estimate the maximum percentage of objects that show evidence for RSFA in the combined 2 Jy and 3CRR sample by considering all the main optical and infrared diagnostics of star formation activity. In order to summarize the results we have collated the data for the various RSFA identifiers in Table 5. Several objects are not complete in terms of the available optical, PAH, far-IR excess, and color tests of RSFA (indicated by a "U" in the Table). However, all the objects have at least two separate pieces of RSFA diagnostic information. We further note that, of the 17 objects with optical, low or high EW PAH, color-based or infrared excess identification of RSFA, 7 objects are identified as RSFA based on all four diagnostics and a further 9 objects on the basis of two diagnostics.

Considering now the full 2Jy+3CRR sample of 63 objects: 19% (13 objects) show unambiguous spectroscopic evidence for RSFA at optical wavelengths; 21% (13) have cool MFIR colors (F(70/F(24) > 5); 14% (9) have high EW PAH emission; and 22% (14) lie more than 0.5 dex (a factor of three) above the regression line fitted to the $L_{70\,\mu\mathrm{m}}$ versus $L_{[\mathrm{O\,III}]}$ correlation. Overall we find that 27% (17) objects show at least one of these indicators. Including in the analysis the objects with low EW PAH detections (five additional objects not identified using the other diagnostics), we estimate that the maximum percentage of radio-loud AGN showing evidence for RSFA in the combined 2 Jy and 3CRR sample is 35%.

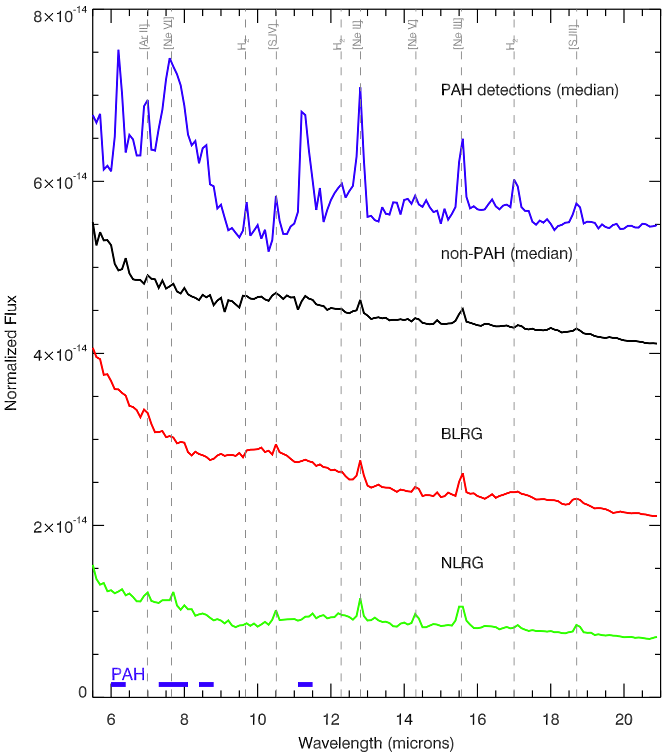

Figure 11. Median spectra for the combined 2 Jy and 3CRR samples; objects with PAH detections (blue), objects without PAH detections (black), BLRG without PAH detections (red), and NLRG without PAH detections (green). The median spectra were normalized at 20 μm and offset in the plot in order to compare them.

(A color version of this figure is available in the online journal.)

This combined result from the various diagnostic methods provides conclusive evidence that a one to one connection between RSFA and AGN activity does *not* exist for the majority of intermediate redshift radio-loud AGN. This conclusion is consistent with our previous investigations, as well as other published *Spitzer* studies in the literature (Tadhunter et al. 2007; D08; D09; Cleary et al. 2007; Shi et al. 2007; Fu & Stockton 2009)

In a study of 33 3C quasars and radio galaxies at high/intermediate redshifts ($0.5 < z < 1.1$), Cleary et al. (2007) concluded that star formation does not contribute significantly to the MFIR emission. This conclusion was based on the 15 μm/30 μm mid-IR flux ratio also used in other investigations (e.g., Brandl et al. 2006).

The study of Shi et al. (2007) used *Spitzer* IRS data to investigate PAH emission in 3CR radio galaxies, as well as other samples of AGN. Eight objects overlap with the 2 Jy and 3CRR samples presented here. The results of Shi et al. (2007) agree with our study, detecting PAH features in only two of the overlapping objects (3C293, 3C321). The exception is 3C33, where we have identified low EW PAH emission that was not identified in Shi et al. (2007). Moreover, only one object out

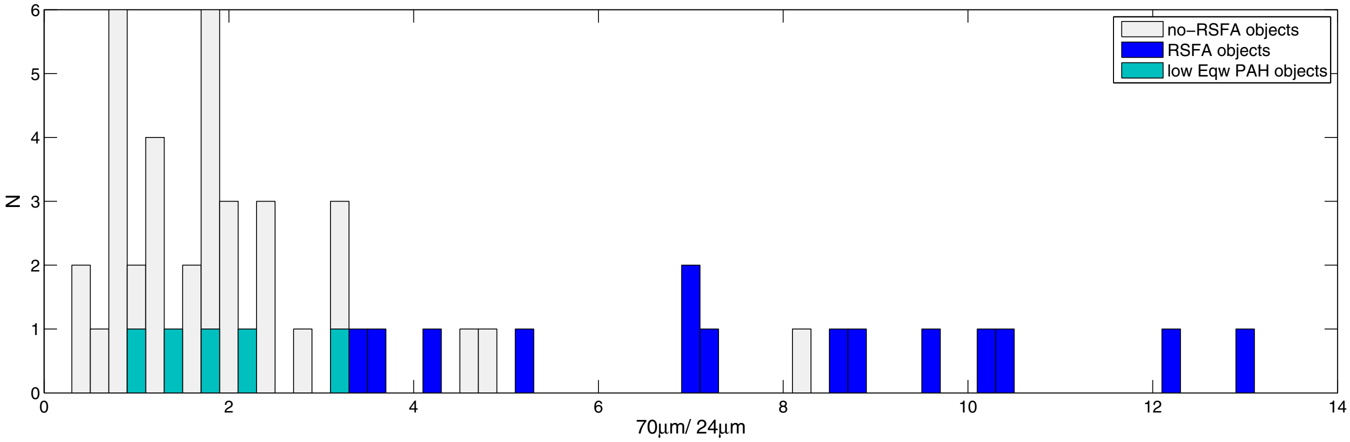

Figure 12. Histogram of 70 μm/24 μm color for the combined 2 Jy and 3CRR sample. Note that the figure does not include the five objects in the 2 Jy sample and the two objects in the 3CRR sample with upper limits on their 70 μm flux.

(A color version of this figure is available in the online journal.)

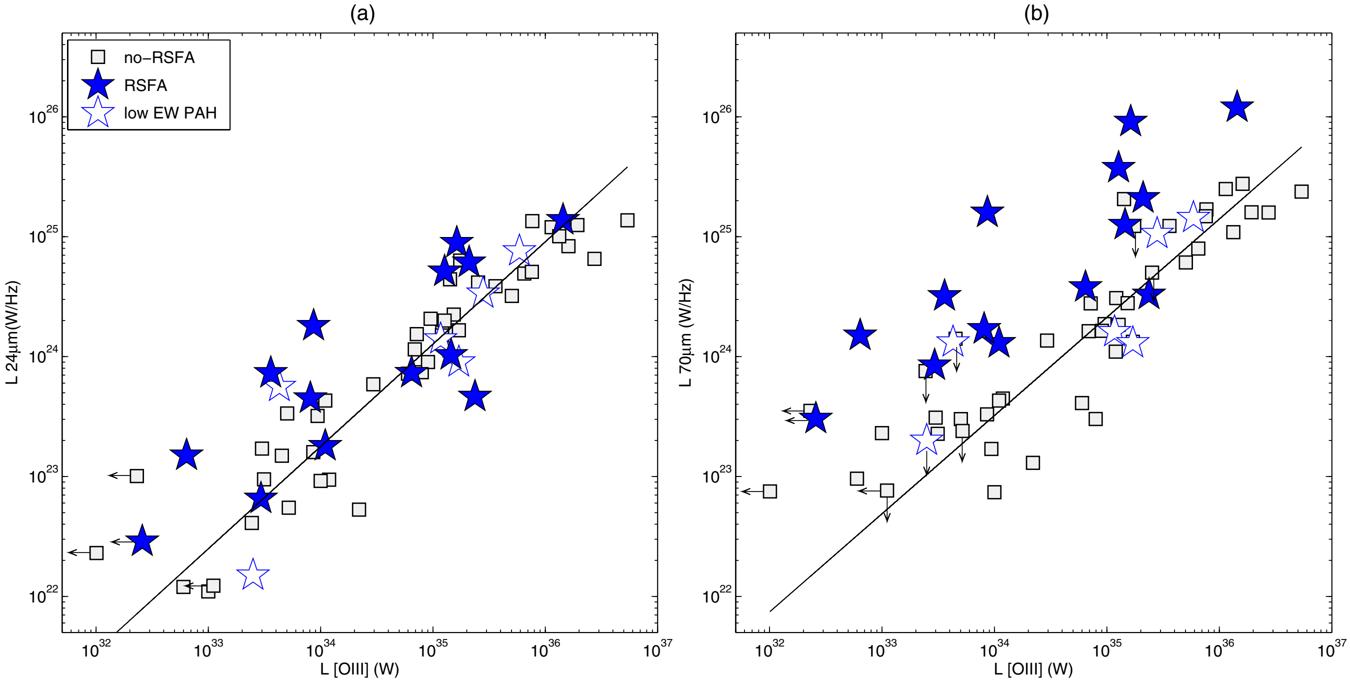

Figure 13. Plot showing $L_{24\,\mu\mathrm{m}}$ and $L_{70\,\mu\mathrm{m}}$ vs. $L_{[\mathrm{O\,III}]}$ where those objects identified to contain evidence for RSFA with optical and/or PAH diagnostics are indicated with blue stars. The lines shown are the bisectors for no-RSFA objects of linear least-squares fits of x on y and y on x. The fits do not include the seven objects with upper limits in either [O III] or 70 μm. The 24 μm, 70 μm, and [O III] fluxes and luminosities for the 2 Jy sample can be found in D08 and D09; fluxes for the 3CRR sample are presented in Dicken et al. (2010).

(A color version of this figure is available in the online journal.)

of the 94 3CR objects included in the Shi et al. (2007) study has both 7.7 and 11.3 μm PAH features detected. Although their sample covers a wider redshift range ($z < 1.5$), and their PAH detection method is likely less sensitive than our study, the results show little evidence for powerful dominant RSFA components in 3CR objects.

Finally, Fu & Stockton (2009) studied a sample of 12 FRII radio-loud quasars with $z \approx 0.3$, a relatively similar sample of objects in terms of redshift to the 2 Jy sample presented in this paper. They found no evidence for PAH emission in any individual object or from combined spectra.

Clearly, based on several studies of the PAH features, as well as the other diagnostics discussed in this paper, there is little evidence for powerful RSFA activity in the majority of radio-loud AGN.

We emphasize that, due to the radio flux limited selection method for the two samples, the higher redshift objects are likely to be more powerful radio-loud AGN. It is conceivable that this bias could affect the detection rate of PAH or other RSFA diagnostics across the redshift range of the sample. However, we find no obvious trend with redshift in terms of the rate of detection of RSFA. For example, the rate of detection of RSFA activity in the low-redshift 3CRR sample ($z \leqslant 0.1$: 36% have optical and/or PAH detection evidence, including low EW PAH detections) is not significantly different from that in the intermediate-redshift 2 Jy sample ($0.05 < z < 0.7$: 28%). This

Table 5
Recent Star Formation Activity Detections in the 2 Jy and 3CRR Samples

Name	Other	Optical	PAH	Color	Far-IR	Name	Other	Optical	PAH	Color	Far-IR
0023−26		✔	✔	✔	✔	1814−63		U	low	. . .	✔
0034−01	3C15	. . .	. . .	. . .	. . .	1839−48		. . .	. . .	. . .	. . .
0035−02	3C17	. . .	. . .	. . .	. . .	1932−46		✔	. . .	✔	. . .
0038 + 09	3C18	. . .	. . .	. . .	. . .	1934−63		. . .	low	. . .	. . .
0039−44		. . .	. . .	. . .	. . .	1938−15		. . .	. . .	. . .	. . .
0043−42		. . .	. . .	. . .	. . .	1949 + 02	3C403	. . .	. . .	. . .	. . .
0105−16	3C32	. . .	. . .	U	. . .	1954−55		. . .	. . .	. . .	. . .
0117−15	3C38	. . .	. . .	. . .	. . .	2135−14		U	U	. . .	. . .
0213−13	3C62	. . .	. . .	. . .	. . .	2135−20	OX–258	✔	✔	✔	✔
0235−19	OD–159	. . .	. . .	. . .	. . .	2211−17	3C444	. . .	U	U	. . .
0252−71		. . .	. . .	U	. . .	2221−02	3C445	. . .	. . .	. . .	. . .
0347 + 05		✔	✔	✔	✔	2250−41		. . .	. . .	. . .	. . .
0349−27		U	. . .	. . .	. . .	2314 + 03	3C459	✔	✔	✔	✔
0404 + 03	3C105	. . .	. . .	. . .	. . .	2356−61		. . .	. . .	. . .	. . .
0409−75		✔	. . .	✔	✔	3C33		. . .	low	. . .	. . .
0442−28		. . .	. . .	. . .	. . .	3C35		. . .	U	U	. . .
0620−52		✔	. . .	✔	. . .	3C98		. . .	. . .	. . .	. . .
0625−35	OH–342	. . .	. . .	. . .	. . .	DA240		. . .	U	✔	✔
0625−53		. . .	. . .	U	. . .	3C192		. . .	. . .	. . .	. . .
0806−10	3C195	. . .	low	. . .	. . .	4C73.08		. . .	U	. . .	. . .
0859−25		. . .	. . .	. . .	. . .	3C236		✔	low	. . .	✔
0915−11	Hydra A	✔	✔	✔	✔	3C277.3		. . .	U	. . .	. . .
0945 + 07	3C227	U	. . .	. . .	. . .	3C285		✔	✔	✔	✔
1136−13		U	. . .	. . .	. . .	3C293		✔	✔	✔	✔
1151−34		U	low	. . .	. . .	3C305		✔	✔	✔	✔
1306−09		U	. . .	. . .	✔	3C321		✔	low	. . .	✔
1355−41		U	. . .	. . .	. . .	3C326		. . .	low	U	. . .
1547−79		U	. . .	. . .	. . .	3C382		U	. . .	. . .	. . .
1559 + 02	3C327	. . .	. . .	. . .	. . .	3C388		. . .	. . .	U	. . .
1602 + 01	3C327.1	. . .	. . .	. . .	. . .	3C390.3		U	. . .	. . .	. . .
1648 + 05	Herc A	. . .	U	U	. . .	3C452		. . .	. . .	. . .	. . .
1733−56		U	✔	✔	. . .						

Notes. RSFA detections for the 2 Jy and 3CRR samples. A dash means that no evidence for RSFA activity exists for that diagnostic method. Optical column: a tick indicates that the object have young stellar populations identified in careful modeling of optical spectra, U (uncertain) identifies objects where it was not possible to model the spectrum effectively. PAH column: a tick indicates positive strong PAH detection, low indicates a low EW or low S/N PAH detection, while U indicates that good IRS spectra are not available. Color column: a tick indicates that an object has 70 μm/24 μm $\gtrsim 5$, U indicates that the object has an upper limit in 70 μm flux. Far-IR column: a tick indicates that the object has a far-IR excess in the sense that it falls 0.5 dex (a factor of three) above the regression line fitted to $L_{70\,\mu\mathrm{m}}$ vs. $L_{[\mathrm{O\,III}]}$ correlation, not including object with upper limits. Note that two of the objects in the 3CRR sample are in common with the 2 Jy sample: 3C403 (PKS1949 + 02), 3C445 (PKS2221−02).

confirms that the diagnostic methods we have employed are consistent across the redshift ranges of the two samples.

6.2. *Ratios of PAH Emission Band Fluxes*

It has been shown, both experimentally and theoretically, that the ratios between the fluxes of the 6.2, 7.7, 8.6, and 11.3 μm PAH emission features are sensitive to the radiation environments of the photodissociation regions in which they are produced, as well as the sizes of the aromatic molecules and the degree to which they have been reprocessed in shocks (Diamond-Stanic & Rieke 2010 and references therein). Since the PAH features are used as a star formation indicator for AGN host galaxies, it is important to investigate whether the PAH emission band spectra are affected by the presence of AGNs.

In an extensive study of the PAH ratios measured for a large sample of Seyfert galaxies from the Revised Shapley–Ames catalogue (RSA), Diamond-Stanic & Rieke (2010) have found that, on average, the Seyfert galaxies show 7.7/11.3 PAH flux ratios that are low compared with local star-forming galaxies, with some Seyfert galaxies identified as having unusually small ratios ($7.7/11.3 < 2$)—lower than measured for any of the local star-forming H II galaxies in the *Spitzer* Infrared Nearby Galaxies Survey (SINGs) sample of Smith et al. (2007). This agrees with previous work that also suggested a link between low 7.7/11.3 ratios and the presence of AGN activity (Smith et al. 2007; O'Dowd et al. 2009). It is therefore interesting to investigate whether the radio galaxies in our sample with high EW PAH emission—which encompass larger AGN luminosities than the Diamond-Stanic & Rieke (2010) sample—also show low 7.7/11.3 ratios.

Referring back to Figure 7, the apparent similarity between PAH spectra of the objects with high EW PAH detections is striking. Considering only the seven objects for which the 6.2, 7.7, and 11.3 μm features can be accurately measured (six objects from the 2 Jy sample and one object from the 3CRR sample) the mean ratios are $6.2/11.3 = 0.7 \pm 0.2$, $7.7/11.3 = 1.7 \pm 0.4$, and $6.2/7.7 = 0.4 \pm 0.1$, see Table 6. It is notable that the 7.7/11.3 ratios measured for the radio galaxies fall at the lower end of the range measured for RSA Seyfert galaxies and the SINGs H II galaxies; two radio galaxies (PKS0023−16, 3C293) have 7.7/11.3 ratios that are comparable with the most extreme Seyfert galaxies measured by Diamond-Stanic & Rieke (2010).

Table 6
PAH Ratios

Name	6.2/11.3	7.7/11.3	6.2/7.7	$H_2(S3)/(11.3 + 7.7)$
0023−26	0.8 ± 0.1	1.2 ± 0.1	0.7 ± 0.1	0.113 ± 0.014
0347 + 05	0.7 ± 0.1	1.8 ± 0.1	0.4 ± 0.1	0.008 ± 0.004
0915−11	0.8 ± 0.1	1.8 ± 0.2	0.4 ± 0.1	0.005 ± 0.003
1733−56	1.0 ± 0.1	1.9 ± 0.2	0.5 ± 0.1	0.008 ± 0.004
2135−20	0.5 ± 0.1	1.9 ± 0.2	0.3 ± 0.1	0.018 ± 0.016
2314 + 03	0.8 ± 0.1	2.4 ± 0.2	0.3 ± 0.1	0.011 ± 0.003
3C293	0.4 ± 0.1	1.2 ± 0.1	0.3 ± 0.1	0.156 ± 0.007

Notes. Table presenting the ratios of PAH and H_2 flux ratios for objects with high EW detections of PAH. See Section 6.2 of the discussion. This table does not include 3C285 and 3C305 that have upper limits for their 6.2 and 7.7 μm PAH fluxes.

Based on the strong correlation they found between 7.7/11.3 ratios and strong $H_2S(3)$ emission, Diamond-Stanic & Rieke (2010) suggested that the low 7.7/11.3 may be due to the reprocessing of the PAH-emitting molecules in shocks, since the rotational $H_2S(3)$ feature is enhanced in relatively hot, shocked regions of the ISM (Guillard et al. 2009; Ogle et al. 2010). Although our sample is too small for a thorough statistical investigation, it is notable in that the objects with the smallest 7.7/11.3 ratio—PKS0023−26 and 3C293—also have the highest ratios of H_2(S3)/(11.3 + 7.7) among all the radio galaxies in the combined 2 Jy and 3CRR sample (see Table 6).

In summary, our results on the PAH ratios for the radio galaxies with RSFA are consistent with those obtained for the most extreme RSA Seyferts studied by Diamond-Stanic & Rieke (2010), reinforcing the view that the 6.6, 7.7, and 8.6 μm features are suppressed relative to the 11.3 μm feature in the environments of AGN, perhaps as a consequence of reprocessing of the aromatic molecules in shocks. Moreover, following the arguments in Diamond-Stanic & Rieke (2010), we would also expect the 11.3 μm feature to be a good indicator of RSFA in radio galaxies, as it is in other classes of AGN.

6.3. The Origin of the Far-IR Emission

Based on the correlations between MFIR and [O III] luminosities, we previously concluded that the cool, far-IR emitting dust is predominantly heated by AGN illumination for the majority of radio galaxies that show no independent evidence for star formation activity (T07; D09; D10). Under the assumption that 11.3 μm PAH luminosity is a measure of the overall level of star formation activity, if the far-IR continuum emission is dominated by AGN-heated dust, then we expect the ratio of the PAH luminosities to the far-IR continuum luminosities to be lower than measured for pure starburst objects. In this vein, Schweitzer et al. (2006) found that the $L_{7.7\,\mu\mathrm{m}}/\nu L\nu_{60\,\mu\mathrm{m}}$ ratio for Palomar–Green (PG) quasars with detected PAH features ($L_{7.7\,\mu\mathrm{m}}/\nu L\nu_{60\,\mu\mathrm{m}} = 0.0110 \pm 0.002$) was similar to that of a sample of 12 starburst-dominated ULIRGs ($L_{7.7\,\mu\mathrm{m}}/\nu L\nu_{60\,\mu\mathrm{m}} = 0.0130 \pm 0.002$), a result that was also discussed by Veilleux et al. (2009). The authors conclude that the similar ratios argue in favor of a starburst origin for the far-IR emission of PG quasars. In contrast, based on similar techniques, Shi et al. (2007) concluded that the contribution of starburst heating to the far-IR continuum is relatively minor (∼24%) for most radio-loud AGN.

The problem with using the $L_{\mathrm{PAH}}/L_{\mathrm{far\text{-}IR}}$ ratio as a direct indicator of the degree of starburst heating of the far-IR emitting dust is that the scatter in this ratio is large, even for starburst-dominated objects. Results from SINGs have indicated that the use of PAH emission for estimating star formation rates may be uncertain by a factor of ∼10 (Dale et al. 2005; Calzetti et al. 2007). This conclusion is also supported by Tacconi-Garman et al. (2005) who find strong variations in the PAH to stellar continuum ratio in nearby starburst galaxies, as well as Haas et al. (2009) who find a range in the $L_{\mathrm{fir}}/L_{6.3\,\mu\mathrm{m}}$ of a factor of 10 for a sample of PAH-selected galaxies from the ISOCAM parallel survey. In Figure 14 we plot $L_{11.3\,\mu\mathrm{m}}/\nu L_\nu 60\,\mu\mathrm{m}$ for the 2 Jy and 3CRR objects from the current study, along with comparison samples of luminous infrared galaxies (LIRGs) and starburst objects of similar far-IR luminosity taken from Brandl et al. (2006), and starburst-dominated ULIRGs taken from the study of Veilleux et al. (2009).

Consistent with the above discussion it is notable that the scatter in the $L_{11.3\,\mu\mathrm{m}}/\nu L_\nu 60\,\mu\mathrm{m}$ ratio is large, both for the radio galaxies we have identified as RSFA objects in our sample, and for the starburst galaxies in the sample of Brandl et al. (2006). In addition, and perhaps counter-intuitively, the

Table 7
Ancillary Data

Name	z	$S_{11.3}$ (W m^{-2})	S_{60} (W Hz^{-1} m^{-2})
	ULIRGs		
F12112+0305	0.0733	8.5E-16	2.5E+26
F17207−0014	0.0428	3.5E-15	2.9E+26
F20414−1651	0.0871	3.6E-16	1.8E+26
F13335−2612	0.1250	3.5E-16	1.3E+26
F03250+1606	0.1290	3.5E-16	1.4E+26
F10565+2448	0.0431	2.8E-15	1.1E+26
F23234+0946	0.1279	1.7E-16	1.7E+26
F14348−1447	0.0830	7.6E-16	2.6E+26
F22491−1808	0.0778	3.1E-16	1.7E+26
F16333+4630	0.1910	3.0E-16	3.4E+26
Arp 220	0.0181	3.5E-15	1.6E+26
F14197+0813	0.1310	1.1E-16	1.1E+26
F05024−1941	0.1920	1.1E-16	2.6E+26
F01494−1845	0.1580	3.5E-16	2.0E+26
F00482−2721	0.1292	9.3E-17	1.1E+26
	LIRGS and starbursts		
IC 342	0.0001	1.8E-14	8.3E+21
Mrk 52	0.0071	2.1E-15	1.1E+24
Mrk 266	0.0155	2.7E-15	7.9E+24
NGC 520	0.0076	2.9E-14	8.1E+24
NGC 660	0.0028	4.9E-14	2.3E+24
NGC 1097	0.0042	4.3E-14	4.2E+24
NGC 1222	0.0082	6.5E-15	3.8E+24
NGC 1365	0.0055	3.0E-14	1.2E+25
NGC 1614	0.0159	1.6E-14	3.6E+25
NGC 2146	0.0030	1.6E-13	5.7E+24
NGC 2623	0.0185	4.2E-15	3.7E+25
NGC 3256	0.0094	4.1E-14	4.0E+25
NGC 3310	0.0033	1.6E-14	1.7E+24
NGC 3556	0.0023	3.0E-14	7.7E+23
NGC 3628	0.0028	3.6E-14	1.9E+24
NGC 4088	0.0025	1.9E-14	7.5E+23
NGC 4194	0.0083	1.6E-14	7.1E+24
NGC 4676	0.0220	3.7E-15	5.9E+24
NGC 4818	0.0036	8.9E-15	1.1E+24
NGC 4945	0.0019	1.9E-13	9.7E+24
NGC 7252	0.0160	6.0E-15	4.6E+24
NGC 7714	0.0093	7.0E-15	4.3E+24

Notes. Table presenting the ancillary data from Figure 14 for ULIRG, LIRG, and starburst objects.

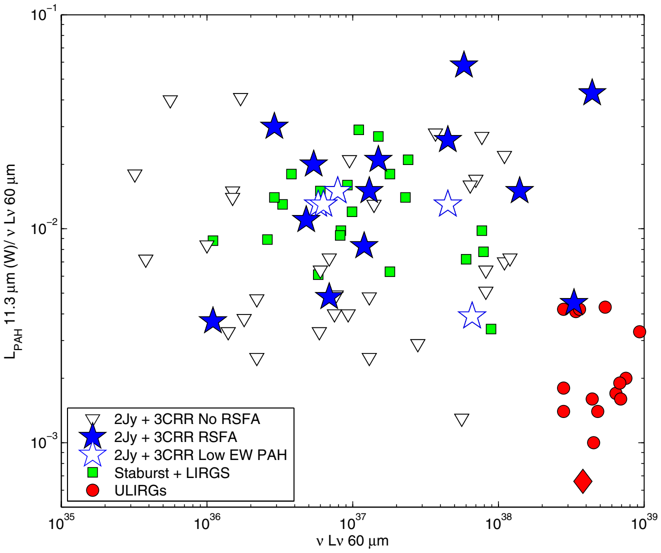

Figure 14. Plot of $L_{11.3\,\mu\mathrm{m}}/\nu L_\nu 60\,\mu$m vs. $\nu L_\nu 60\,\mu$m. The 60 μm fluxes for the starburst and LIRG galaxies were obtained from the IRAS catalogue, and the 2 Jy and 3CRR sample 70 μm fluxes were interpolated to 60 μm using the 70/24 μm spectral index from the *Spitzer* data. The IRS data for the starburst galaxies and ULIRGs were downloaded from the *Spitzer* Heritage Archive and re-reduced and analyzed in an identical way as described for the radio galaxies in this paper. In addition, to compensate for flux loss in the IRS spectra due to the extended structure of the starburst and LIRG galaxies outside of the slit, a correction factor was applied as discussed in Brandl et al. (2006). The ULIRG sample comprises 15 objects from the sample presented in Veilleux et al. (2009) with an average AGN contribution of <20%. The archetypal ULIRG ARP220 is marked with a red diamond. The 11.2 μm PAH fluxes measured for the starburst, LIRGs and starburst-dominated ULIRGs are presented in Table 7, along with the IRAS 60 micron fluxes.

(A color version of this figure is available in the online journal.)

starburst-dominated ULIRGs tend to the lowest values of $L_{11.3\,\mu\mathrm{m}}/\nu L_\nu 60\,\mu$m. An explanation for this difference might be that a significant fraction of the starburst activity in the ULIRGs is so deeply embedded and extinguished by dust that it is not detected using the short-wavelength PAH features (see Veilleux et al. 2009 for further discussion).

Given the high degree of scatter and large number of relatively high upper limits in the plot, it is difficult to make strong conclusions about the heating mechanism for the far-IR emitting dust for most of the radio galaxies in our sample based on this evidence alone. However, the upper limits for some radio galaxies fall well below the majority of values measured for the Brandl et al. LIRG and starburst galaxies ($L_{11.3\,\mu\mathrm{m}}/\nu L_\nu 60\,\mu\mathrm{m} < 5 \times 10^{-3}$), suggesting that AGN illumination makes a large contribution to the heating of the cool dust in these objects, supporting our previous conclusions (T07; D09). It is noteworthy that many of the objects with $L_{\mathrm{PAH}11.3\,\mu\mathrm{m}}/\nu L_\nu\ 60\,\mu\mathrm{m} < 5 \times 10^{-3}$ comprise the low-z NLRG with high S/N spectra (e.g., PKS1559+02, PKS1949+02, PKS2250−41, PKS2356−61) as well as low-z BLRG (3C382, 3C390.3) with the very highest S/N spectra. This suggests that many of the objects with low S/N spectra (mainly high-z objects) might fall in this region of the diagram if they had better S/N data.

These results are relevant to the interpretation of the far-IR emission from AGN in the distant universe. High-redshift galaxies that show evidence for AGN activity at X-ray (Alexander et al. 2005), optical (Priddey et al. 2003), and radio (Archibald et al. 2001; Willott et al. 2002) wavelengths have been detected with deep surveys at submillimeter wavelengths which are sensitive to the redshifted far-IR emission from cool dust. Because investigations of starburst galaxies in the local universe have revealed prodigious far-IR radiation, the submillimeter emission has been interpreted as being due to cold dust heated by strong star formation activity. Our previous work on the 2 Jy sample (T07; D09; D10) has shown that this interpretation is not unique because the dust emitting the thermal MFIR radiation can be heated by either starbursts or by AGN. Figure 14 provides evidence that, in many powerful radio galaxies, far-infrared emission is dominated by AGN and not starburst heating. Therefore, our results suggest that the interpretation of submillimeter emission from distant radio galaxies as originating purely from star formation should be treated with caution.

6.4. Compact Radio Sources

CSS and GPS are characterized by the small sizes of their radio structures ($D < 30$ kpc and <1 kpc, respectively) and steep high-frequency radio spectra. Mounting evidence supports the idea that CSS/GPS objects represent a young phase of more extended powerful radio-loud AGN (Fanti et al. 1995; Readhead et al. 1996). In particular, the measured proper motions of the radio components in some CSS objects that imply very young ages ($<3 \times 10^3$ yr; e.g., Polatidis & Conway 2003).

The combined 2 Jy and 3CRR sample includes seven CSS sources and one GPS source (PKS1934−63). Three of these objects have high EW PAH detections (PKS0023−26, 3C305, PKS2135−20) and three additional objects have been identified with low EW PAH detections (PKS1151−34, PKS1814−63, PKS1934−63). The rate of CSS/GPS objects in the 2Jy+3CRR sample with PAH detections is therefore 75% (6/8)—much higher than the detection rate for the extended radio sources in the 2Jy+3CRR sample with good IRS spectra (21%: 10/48). Interestingly, similar results have been obtained by Willett et al. (2010), who detect PAH emission in 7/8 (88%) of the objects in their heterogeneous sample of nearby compact symmetric objects[19] ($z < 0.26$). This evidence for an enhanced degree of star formation in the host galaxies of compact radio sources is also consistent with the fact that the compact sources are disproportionately represented in the (small) subset of radio galaxies that show strong evidence for young stellar populations in their optical spectra (Tadhunter et al. 2011).

At first sight it might be thought that the relatively high incidence of starburst activity among the compact radio sources is connected with the relative youthfulness of such sources: if the radio source activity is triggered close to the peak of the starburst associated with the triggering events, then the compact sources might be expected to show enhanced star formation activity compared to the more extended radio sources that are observed at later epochs. However, the problem with this explanation is that both models (Mihos & Hernquist 1996; Di Matteo et al. 2007) and direct observations (Rodríguez Zaurín et al. 2010) suggest that the main starburst episodes associated with major galaxy mergers are relatively long-lived: ∼10–100 Myr—much longer than the expected time period over which a radio source would appear as a compact radio source, but similar to expected lifetimes of extended radio sources. Moreover, the spectroscopic signatures of the merger-induced starburst would be detectable in optical spectra for several hundred Myr after the starburst. Therefore, we would not expect to find a major difference

---

[19] The CSOs represent a subset of the compact radio source population with relatively symmetric radio structures; most of the compact (CSS, GPS) sources in the 2Jy+3CRR sample would also be classified as CSOs.

between the rate of detection of starburst signatures in compact and extended radio sources, given the similarities between the expected timescales of (extended) radio sources and starburst activity.

Alternatively, Tadhunter et al. (2011) have suggested that the association between starburst activity and compact radio sources may be a consequence of an observational selection effect: young radio sources triggered in major gas-rich mergers, that also lead to starbursts, will have their radio emission enhanced by jet/cloud interactions as their radio jets plough through the dense merger debris. This will lead to such sources being preferentially selected in flux limited radio samples such as the 2 Jy and 3CRR, boosting their numbers relative to the radio sources that are not triggered in major gas-rich mergers; the compact radio sources triggered in this way will have a higher ratio of radio power to intrinsic jet and AGN power than more extended radio sources triggered in less dense environments. As these compact sources expand further into the more tenuous halos of the host galaxies their radio fluxes will decline and they will drop out of the flux limited samples. We note that this selection effect is consistent with the fact that the compact radio sources tend to fall below the correlations between [O iii] and 24 μm emission and radio power, as expected if the radio flux is boosted relative to the intrinsic AGN power (Morganti et al. 1997; Holt et al. 2009; Morganti et al. 2011). It may also help explain why O'Dea & Baum (1997) found evidence that compact radio sources are more common in flux limited radio samples than would be expected on the basis of a simple extrapolation of the radio size versus number relation for more extended radio sources.[20]

6.5. Consequences for the Triggering and Evolution of Radio Source Host Galaxies

In parallel work, we have found that at least 85% of the objects in the 2 Jy sample show morphological evidence for recent galaxy interactions and mergers (Ramos Almeida et al. 2011, 2012). However, the morphologies and stellar population properties displayed by the radio source host galaxies are diverse and do not all correspond to a single phase of a particular type of galaxy interaction (Ramos Almeida et al. 2011, 2012; Tadhunter et al. 2011). While some radio sources have indeed clearly been triggered at the peaks of major gas-rich mergers, others are seen at a relatively late post-merger phases well *after* the coalescence of the merging nuclei; and a significant subset shows tidal links with well-separated companion galaxies, suggesting that they have been triggered after the first pass of the interacting galaxies, but well *before* the final merger (if any). These results indicate that it is possible for the gas inflows associated with a range of stages and types of galaxy interactions to be sufficient to trigger powerful radio galaxies, many of which are associated with AGN of quasar-like luminosity ($L_{\mathrm{BOL}} > 10^{38}$ W). Overall, these results are inconsistent with many recent hydrodynamical simulations which predict that the most powerful, quasar-like AGN activity is only triggered around the time of coalescence of the merging nuclei in major, gas-rich mergers (e.g., di Matteo et al. 2005), or with a short time delay (Hopkins 2011). Our mid-IR results on the PAH features strongly reinforce these conclusions: in most objects we do not detect the levels of RSFA that would be expected if all powerful radio galaxies were triggered at the peaks of major, gas-rich mergers.[21] We suggest that the current hydrodynamical simulations do not adequately capture the physics of the gas flows across the variety of interaction types and/or stages that lead to the triggering of radio-loud AGN.

It is also important to consider whether the negative feedback effect of the AGN and jet activity might be responsible for the low levels of RSFA detected in radio galaxies, i.e., whether the AGN and jets in these powerful radio galaxies input sufficient energy into the ISM of the host galaxies to suppress some of the star formation associated with the triggering events. Because star formation associated with advanced mergers is often concentrated near the nucleus, the energy input of the AGN may have a major impact on these star formation regions. Given that we have found evidence for RSFA in up to 35% of our samples, it appears that the AGN cannot entirely shut down star formation in powerful radio galaxies. On the other hand, we note that two of the objects in this investigation (3C293, 3C326) have been associated with AGN feedback processes through detailed observations of the molecular gas content. The study of Nesvadba et al. (2010) found evidence that these objects have star formation rates lower than expected for the amount of dense gas available for star formation.

The feedback effect of the AGN may be significant in some objects, however, the lack of evidence for RSFA in the 2 Jy and 3CRR samples may simply be due to the fact that we are observing the sources a long time before or after any main merger-induced starburst. Alternatively, the triggering galaxy interactions may not be of the types that are associated with major star formation episodes (e.g., they may be relatively minor or gas-poor). Clearly, in order to develop our understanding of the triggering events further, we require information about the total reservoir of cool ISM in the host galaxies, as well as the details of the circumnuclear gas kinematics.

7. CONCLUSIONS

We have presented *Spitzer*/IRS spectroscopy for complete samples of 2 Jy and 3CRR radio-loud AGN, detecting 93% and 79% of the objects in the two samples, respectively. Our analysis of the spectra reveals strong RSFA-tracing PAH features in only a minority of the objects from the two samples (16%) that have good IRS spectra. Combining this result with optical continuum spectroscopy, MFIR color and far-IR excess diagnostics, we find that only 35% of objects in the combined 2 Jy and 3CRR sample show any evidence for RSFA at optical and/or MFIR wavelengths. *This result argues strongly against the idea that there is a close link between starbursts and powerful radio-loud AGN, reinforcing the view that only a minority are triggered at the peaks of star formation activity in major, gas-rich mergers.* The PAH emission also allows us to test whether there exists a substantial proportion of RSFA that is obscured by dust that was undetected at optical wavelengths. Although we have found evidence for PAH emission in four objects that were not previously identified as hosting RSFA on the basis of optical spectroscopy, this does not substantially change the statistics for the overall rate of detection of RSFA in radio galaxies from

---

[20] Whereas the extended radio sources ($D > 10$ kpc) show a rapid increase in number within bins of increasing linear size for the radio sources, the compact radio sources ($D < 10$ kpc) show a constant number with size—there are far more compact sources than expected on the basis of a simple extrapolation of the number versus size relationship for the extended sources (see O'Dea & Baum 1997, Figure 10) toward small sizes.

[21] Note that we find no clear link between those objects we have identified in this study with evidence for RSFA and any one particular stage or type of interaction (i.e., with signatures of pre-coalescence, coalescence, and post-coalescence) that have been identified in the host galaxy morphologies.

our previous investigations. In addition, we find that compact radio sources show a significantly higher incidence of RSFA, which cannot be readily explained by the youthful nature of these objects. We suggest that, for radio selected samples, there may be a bias toward the selection of compact radio sources that are triggered in gas-rich environments.

We thank Jack Gallimore for assistance with the modification of PAHFIT. We also thank the anonymous referee for their comments which have improved this investigation. This work is based (in part) on observations made with the *Spitzer Space Telescope*, which is operated by the Jet Propulsion Laboratory, California Institute of Technology under a contract with NASA. This research has made use of the NASA/IPAC Extragalactic Database (NED) which is operated by the Jet Propulsion Laboratory, California Institute of Technology, under contract with NASA. D.D. acknowledges support from NASA grant based on observations from Spitzer program 50588 and the NASA ROSES ADAP program. M.B.N.K. was supported by the Peter and Patricia Gruber Foundation through the IAU-PPGF fellowship, by the Peking University One Hundred Talent Fund (985), and by the National Natural Science Foundation of China (grants 11010237 and 11043007). C.R.A. acknowledges financial support from STFC PDRA (ST/G001758/1). K.J.I. is funded through the Emmy Noether Programme of the German Science Foundation (DFG).

Facility: Spitzer (IRS)

REFERENCES

Alexander, D. M., Smail, I., Bauer, F. E., et al. 2005, Nature, 434, 738
Archibald, E. N., Dunlop, J. S., Hughes, D. H., et al. 2001, MNRAS, 323, 417
Benson, A. J., Bower, R. G., Frenk, C. S., et al. 2003, ApJ, 599, 38
Best, P. N., Kaiser, C. R., Heckman, T. M., & Kauffmann, G. 2006, MNRAS, 368, L67
Best, P. N., Kauffmann, G., Heckman, T. M., et al. 2005, MNRAS, 362, 25
Bower, R. G., Benson, A. J., Malbon, R., et al. 2006, MNRAS, 370, 645
Brandl, B. R., Bernard-Salas, J., Spoon, H. W. W., et al. 2006, ApJ, 653, 1129
Buttiglione, S., Capetti, A., Celotti, A., et al. 2009, A&A, 495, 1033
Calzetti, D., Kennicutt, R. C., Engelbracht, C. W., et al. 2007, ApJ, 666, 870
Cleary, K., Lawrence, C. R., Marshall, J. A., Hao, L., & Meier, D. 2007, ApJ, 660, 117
Cox, T. J., Jonsson, P., Somerville, R. S., Primack, J. R., & Dekel, A. 2008, MNRAS, 384, 386
Croton, D. J., Springel, V., White, S. D. M., et al. 2006, MNRAS, 365, 11
Dale, D. A., Bendo, G. J., Engelbracht, C. W., et al. 2005, ApJ, 633, 857
di Matteo, P., Capuzzo Dolcetta, R., & Miocchi, P. 2005, Celest. Mech. Dyn. Astron., 91, 59
Di Matteo, P., Combes, F., Melchior, A., & Semelin, B. 2007, A&A, 468, 61
di Serego-Alighieri, S., Danziger, I. J., Morganti, R., & Tadhunter, C. N. 1994, MNRAS, 269, 998
Diamond-Stanic, A. M., & Rieke, G. H. 2010, ApJ, 724, 140
Dicken, D., Tadhunter, C., Axon, D., et al. 2009, ApJ, 694, 268
Dicken, D., Tadhunter, C., Axon, D., et al. 2010, ApJ, 722, 1333
Dicken, D., Tadhunter, C., Morganti, R., et al. 2008, ApJ, 678, 712
Fanti, C., Fanti, R., Dallacasa, D., et al. 1995, A&A, 302, 317
Fu, H., & Stockton, A. 2009, ApJ, 696, 1693
Gallimore, J. F., Yzaguirre, A., Jakoboski, J., et al. 2010, ApJS, 187, 172
Guillard, P., Boulanger, F., Pineau Des Forêts, G., & Appleton, P. N. 2009, A&A, 502, 515
Haas, M., Leipski, C., Siebenmorgen, R., et al. 2009, A&A, 507, 713
Hao, L., Weedman, D. W., Spoon, H. W. W., et al. 2007, ApJ, 655, L77
Heckman, T. M., Miley, G. K., Balick, B., van Breugel, W. J. M., & Butcher, H. R. 1982, ApJ, 262, 529
Heckman, T. M., Smith, E. P., Baum, S. A., et al. 1986, ApJ, 311, 526
Higdon, S. J. U., Devost, D., Higdon, J. L., et al. 2004, PASP, 116, 975
Holt, J., Tadhunter, C. N., González Delgado, R. M., et al. 2007, MNRAS, 381, 611
Holt, J., Tadhunter, C. N., & Morganti, R. 2008, MNRAS, 387, 639
Holt, J., Tadhunter, C. N., & Morganti, R. 2009, MNRAS, 400, 589
Hopkins, P. F. 2011, arXiv:1101.4230
Houck, J. R., Roellig, T. L., Van Cleve, J., et al. 2004, Proc. SPIE, 5487, 62
Inskip, K. J., Tadhunter, C. N., Morganti, R., et al. 2010, MNRAS, 407, 1739
Isobe, T., Feigelson, E. D., & Nelson, P. I. 1986, ApJ, 306, 490
Johansson, P. H., Naab, T., & Burkert, A. 2009, ApJ, 690, 802
Kaneda, H., Onaka, T., Sakon, I., et al. 2008, ApJ, 684, 270
Laing, R. A., Riley, J. M., & Longair, M. S. 1983, MNRAS, 204, 151
LaMassa, S. M., Heckman, T. M., Ptak, A., et al. 2010, ApJ, 720, 786
Lavalley, M., Isobe, T., & Feigelson, E. 1992, in ASP Conf. Ser. 25, Astronomical Data Analysis Software and Systems I, ed. D. M. Worrall, C. Biemesderfer, & J. Barnes (San Francisco, CA: ASP), 245
Lebouteiller, V., Bernard-Salas, J., Sloan, G. C., & Barry, D. J. 2010, PASP, 122, 231
McNamara, B. R., & Nulsen, P. E. J. 2007, ARA&A, 45, 117
Mihos, J. C., & Hernquist, L. 1996, ApJ, 464, 641
Morganti, R., Holt, J., Tadhunter, C., et al. 2011, A&A, 535, 97
Morganti, R., Killeen, N. E. B., & Tadhunter, C. N. 1993, MNRAS, 263, 1023
Morganti, R., Oosterloo, T., Tadhunter, C. N., et al. 1999, A&AS, 140, 355
Morganti, R., Oosterloo, T. A., Reynolds, J. E., Tadhunter, C. N., & Migenes, V. 1997, MNRAS, 284, 541
Nesvadba, N. P. H., Boulanger, F., Salomé, P., et al. 2010, A&A, 521, A65
O'Dea, C. P., & Baum, S. A. 1997, AJ, 113, 148
O'Dowd, M. J., Schiminovich, D., Johnson, B. D., et al. 2009, ApJ, 705, 885
Ogle, P., Boulanger, F., Guillard, P., et al. 2010, ApJ, 724, 1193
Polatidis, A. G., & Conway, J. E. 2003, PASA, 20, 69
Priddey, R. S., Isaak, K. G., McMahon, R. G., & Omont, A. 2003, MNRAS, 339, 1183
Ramos Almeida, C., Bessiere, P. S., Tadhunter, C. N., et al. 2012, MNRAS, 419, 687
Ramos Almeida, C., Tadhunter, C. N., Inskip, K. J., et al. 2011, MNRAS, 410, 1550
Rawlings, S., & Saunders, R. 1991, Nature, 349, 138
Readhead, A. C. S., Taylor, G. B., Pearson, T. J., & Wilkinson, P. N. 1996, ApJ, 460, 634
Rieke, G. H., Young, E. T., Engelbracht, C. W., et al. 2004, ApJS, 154, 25
Rodríguez Zaurín, J., Tadhunter, C. N., & González Delgado, R. M. 2010, MNRAS, 403, 1317
Schweitzer, M., Lutz, D., Sturm, E., et al. 2006, ApJ, 649, 79
Shi, Y., Ogle, P., Rieke, G. H., et al. 2007, ApJ, 669, 841
Simpson, C. 1998, MNRAS, 297, L39
Smith, J. D. T., Draine, B. T., Dale, D. A., & Moustakas, J. 2007, ApJ, 656, 770
Tacconi-Garman, L. E., Sturm, E., Lehnert, M., et al. 2005, A&A, 432, 91
Tadhunter, C., Dicken, D., Holt, J., et al. 2007, ApJ, 661, L13
Tadhunter, C., Dickson, R., Morganti, R., et al. 2002, MNRAS, 330, 977
Tadhunter, C., Holt, J., González Delgado, R., et al. 2011, MNRAS, 412, 960
Tadhunter, C., Robinson, T. G., González Delgado, R. M., Wills, K., & Morganti, R. 2005, MNRAS, 356, 480
Tadhunter, C. N., Morganti, R., di Serego-Alighieri, S., Fosbury, R. A. E., & Danziger, I. J. 1993, MNRAS, 263, 999
Tadhunter, C. N., Morganti, R., Robinson, A., et al. 1998, MNRAS, 298, 1035
Veilleux, S., Rupke, D. S. N., Kim, D., et al. 2009, ApJS, 182, 628
Villar-Martín, M., Tadhunter, C., Morganti, R., & Holt, J. 2005, MNRAS, 359, L5
Wall, J. V., & Peacock, J. A. 1985, MNRAS, 216, 173
Willett, K. W., Stocke, J. T., Darling, J., & Perlman, E. S. 2010, ApJ, 713, 1393
Willott, C. J., Rawlings, S., Archibald, E. N., & Dunlop, J. S. 2002, MNRAS, 331, 435
Wills, K. A., Morganti, R., Tadhunter, C. N., Robinson, T. G., & Villar-Martin, M. 2004, MNRAS, 347, 771
Wills, K. A., Tadhunter, C., Holt, J., et al. 2008, MNRAS, 385, 136
Wills, K. A., Tadhunter, C. N., Robinson, T. G., & Morganti, R. 2002, MNRAS, 333, 211